$CuO/g\text{-}C_3N_4$ Catalysts for Highly Selective Electrochemical CO_2 Reduction to C_2 Products

Zijun YAN

Student ID: 20415357

Department of Chemical and Environmental Engineering

University of Nottingham Ningbo China

Submitted September 2022, in partial fulfilment of the conditions of the award of the degree MRes. in Environmental Science and Engineering

I hereby declare that this dissertation is all my own work, except as indicated in the text:

Signature: _____

Date: _____/_____/____

Abstract

Environmental dangers and a change in the world's climate are being brought on by the atmosphere's constant increase in CO_2 concentration. The transformation of CO_2 into gasoline or manufacture feedstock by photochemical, electrochemical, thermochemical and biochemical methods using recoverable power sources to improve the human climate system is an important means to solve this problem. In particular, electrochemical CO_2 reduction (CO_2R) has become an attractive and promising pathway due to its advantages of being more energy-saving and sustainable. However, CO_2 is a stable linear molecule and the electrochemical CO_2R process is a multi-step effect involving multi-nucleus transformations, so it is very challenging to transform CO_2 into C_2 and C_{2+} brands with higher energy densities. The transformation of CO_2 to polycarbonate products is only significantly catalyzed by copper according to research, due to its moderate binding strength to *CO intermediates enabling further reaction of *CO intermediates to generate C_2 and C_{2+} products. Herein, in this dissertation, copper oxide/graphite phase carbon nitride ($CuO/g\text{-}C_3N_4$) composite was designed and prepared to improve the electrochemical CO_2R activity as well as the capacity of producing C_2. The $CuO/g\text{-}C_3N_4$ composite was produced by wet chemical assisted hydrothermal processing in alkaline conditions using copper nitrate as the precursor, while the $g\text{-}C_3N_4$ was produced by heat treatment using urea. The composite is based on $g\text{-}C_3N_4$ with homogeneous distribution of polycrystalline copper oxide on it, which can synergistically adsorb and activate CO_2 and thus achieving high specificity of C_2 products. The Faradaic efficiency reaches 37.0 % for C_2H_4 in

an H-type electrolytic cell and 64.7 % for all C_2 products at -1.0 V vs. RHE. The partial current density is about 14 mA cm^{-2} for C_2H_4. In contrast, the Faradaic efficiency of pure CuO nanosheets is 31.7 % for C_2H_4 under the same electrolytic conditions. The findings suggest that the interaction between CuO and the two dimensional g-C_3N_4 planes, which promotes CO_2 adsorption activation and C-C coupling, is the cause of high C_2 selectivity of the CuO/g-C_3N_4 composite. This research offers a practical technique to enhance the activity of electrochemical CO_2R as well as the capacity of generation of C_2 products through synergistic effects.

Keywords: Electrochemical reduction of CO_2, Graphite phase carbon nitride, Copper oxide, C_2 products

Acknowledgements

Accomplishing my goals of graduate study could not have been done alone. Only through the skills, wisdom, and compassion of others could I realize my dreams here. I want to express my heartfelt love and respect to them for everything.

I want to start by expressing my profound thanks to my lead supervisor, Prof. Tao Wu. It is a great honor for me to complete the study successfully under his meticulous guidance. From the design of the technical route to the analysis of the experimental results, Prof. Wu has given me the unremitting support. Apart from that, I'm grateful to the financial and academic support from my other supervisors, i.e., Dr. Yipei Chen.

Moreover, I would express my appreciation to Ms. Jane Zhang, Ms. Helen Xu, Mr. Julian Zhu and Mr. Jason Wang for their assistance and guidance in the trials. Besides, I am deeply indebted to the teachers (Dr. Xiang Luo, Dr. Shuai Liu and Mr. Gang Yang) and some PhD candidates (Ms. Quhan Chen, Ms. Xinyi Mao, Mr. Huiwen Zhu and Mr. Zeyu Guo) for their assistance. In addition, I also want to thank colleagues from New Materials Institute and China Beacon Institute. Finally, I deeply appreciate my parents for their selfless support. Without their encouragement, I could not make progress and overcome difficulties to finish my studies successfully.

TABLE of CONTENT

LIST of FIGURES

LIST of TABLES

CHAPTER I. INTRODUCTION

1.1 Motivation and Strategies for CO_2 Recycling

The conversion of low valence carbon to carbon dioxide, particularly in chemical and energy facilities, is the primary form of carbon oxidation, which is essential to the advancement of human civilization (Nitopi et al., 2019). According to statistics, the burning of fossil fuels produces in excess of thirty billion tonnes of CO_2 per year. The release of CO_2 from human activities along with the depletion of a lot of coal and oil have risen the level of CO_2 in the air, which now exceeds 390 ppm, exceeding the designated safe limit of 350 ppm. This has led to global warming and other adverse effects (Falkowski et al., 2000, Pires et al., 2011). In just the past 30 years, the air temperature of the Planet's surface has climbed by 0.6 °C, posing a serious threat to human survival (Goeppert et al., 2012). In 2015, the Paris Agreement concluded years of negotiations and reset international climate policy goals to keep warming to well below 2 ℃ and eventually to 1.5 ℃ by the end of 21st century. (Rogelj et al., 2019).

For purpose of mitigating the greenhouse effect and minimizing the level of greenhouse gas in the air, the Paris Agreement is being implemented in all regions of the world and a number of measures to reduce CO_2 emissions have been developed. However, it is challenging to drastically reduce the industrial demand for fossil fuels like coal and oil in a short amount of time, and it is inevitable that CO_2 emissions will continue to increase. Therefore, excessive CO_2 emissions cannot simply be banned (Cawley, 2011).

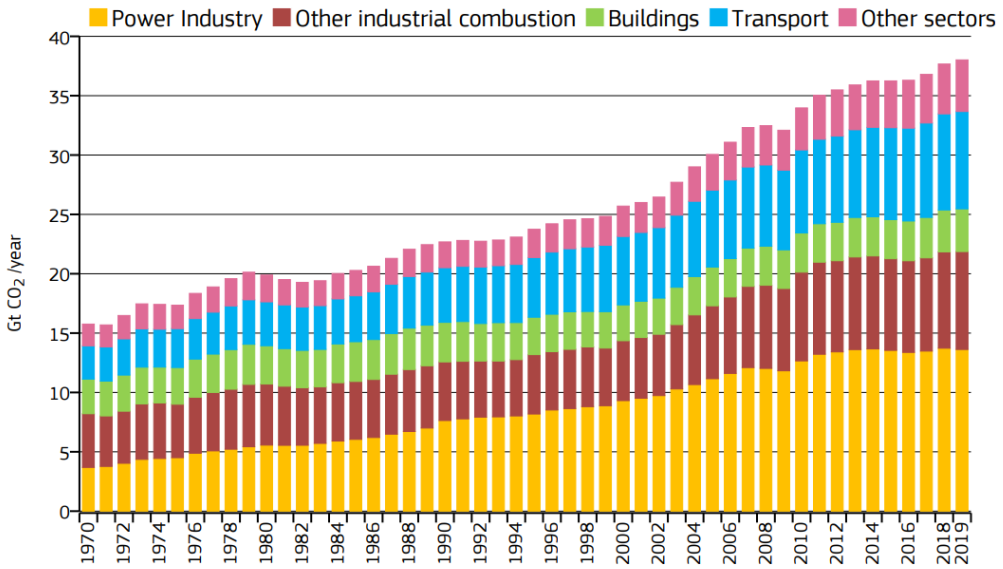

Figure 1.1 Total emissions of fossil CO_2 worldwide per year by sector, expressed in Gt CO_2/yr (Crippa et al., 2020).

Sequestration and utilization of carbon dioxide have received much attention and focus from researchers in recent years (Kohl, 2010, Olah et al., 2011, Orr Jr, 2009), such as carbon capture and sequestration (CCS) technology. CCS is the term for the capture and compression of CO_2 from industrial or other production activities by means of reversible chemisorption, physical adsorption or membrane separation, and is transported to deep underground and store with pipelines or ships (Siegelman et al., 2019). However, there are many roadblocks that must be countered before CCS technologies can advance, including the high cost of capture and storage compression (Bui et al., 2018). Nevertheless, based on the International Energy Agency's blueprint scenario, CCS could account for 19% of global emissions reductions by 2050 (Kohl, 2010), which could be a good transitional phase measure before the full use of sustainable power sources (e.g. solar energy and wind power, etc.).

Utilization of carbon dioxide is primarily a chemical transformation of CO_2 into high-value carbon-containing chemicals for artificial carbon cycling, with much lower reaction costs and higher safety and benefits than CCS technologies (Kondratenko et al., 2013, Nielsen et al., 2018). CO_2 recovery immobilizes intermittent sources of energy into chemical production factors, allowing renewable electricity to be stored in a dense form, greatly highlighting the value of capturing CO_2 from polluting sources (Nitopi et al., 2019). There are three main types of CO_2 catalytic reduction pathways in focus at this stage: thermal catalytic reduction, which is relatively well studied, and the other two are relatively new: photocatalytic reduction and electrocatalytic reduction. Among thermal catalysis, several homogeneous and multiple catalysts have been used for CO_2 hydrogenation and reached industrial level, such as Cu/SiO_2 composite catalysts for CO and $Cu\text{-}ZnO/Al_2O_3$ composite catalysts for methanol (Bansode and Urakawa, 2014, Chen et al., 2003). Photocatalytic CO_2 reduction converts CO_2 and H_2O directly to hydrocarbons using light drive (Fu et al., 2018a, Li et al., 2016a), which can produce methane, carbon monoxide, ethane, methanol, acetaldehyde, etc. (AlOtaibi et al., 2015, Lu et al., 2017, Meng et al., 2018, Niu et al., 2014, Yu et al., 2018). Although the reaction is able to be driven by natural light, it is hard to achieve humongous industrialization due to the high fuel required for catalyst activation and the low reactivity and selectivity of the light-generated electron-hole pairs that tend to compound and deactivate (Fu et al., 2020). Contrarily, electrocatalysis uses clean energy generated by electrical energy and reacts in an aqueous solution at room temperature and pressure under mild reducing conditions. As a result, it

is environmentally friendly and transforms CO_2 into fuels and chemical materials with significant added value while using little energy.

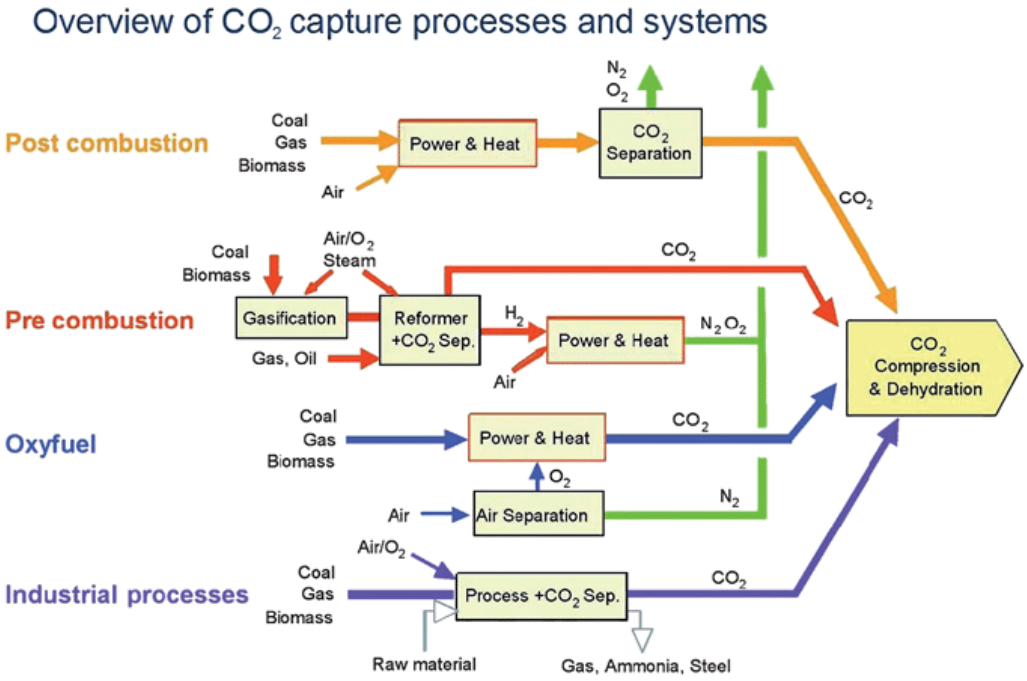

Figure 1.2 CO_2 capture options (Orr Jr, 2009).

1.2 Introduction of Electrochemical CO_2 Reduction

1.2.1 Development History of Electrochemical CO_2 Reduction

The earliest research into CO_2R dates back to 1869, when salicylic acid was produced from CO_2 (Teeter and Van Rysselberghe, 1954). As the cost of renewable electricity has fallen, electrochemical CO_2R has received increasing attention. Inorganic materials have been dominant in CO_2R research. From the beginning of the last century, the electrochemical CO_2R properties of various metallic materials that can convert CO_2 to formate ($HCOO^-$), such as mercury, zinc, copper and lead, began to be investigated. In 1980s, semiconductors such as Ru were found to transform CO_2 to CH_3OH (Benson et al., 2009, Proietto et

al., 2018, Summers and Frese, 1988). In 1986, Hori et al. examined the ability of metallic copper to convert carbon dioxide into hydrocarbons like CH_4 and C_2H_4 as well as the impact of heat flux on the Faradaic efficiency for CH_4 and C_2H_4. (Hori et al., 1986). Over the next two decades, Hori et al. revealed the influence of crystalline surface, element type, electrolyte type and pressure on the selectivity and efficiency of CO_2R products (Hori et al., 1989, Hori et al., 1988, Hori et al., 2002, Hori et al., 1994) .

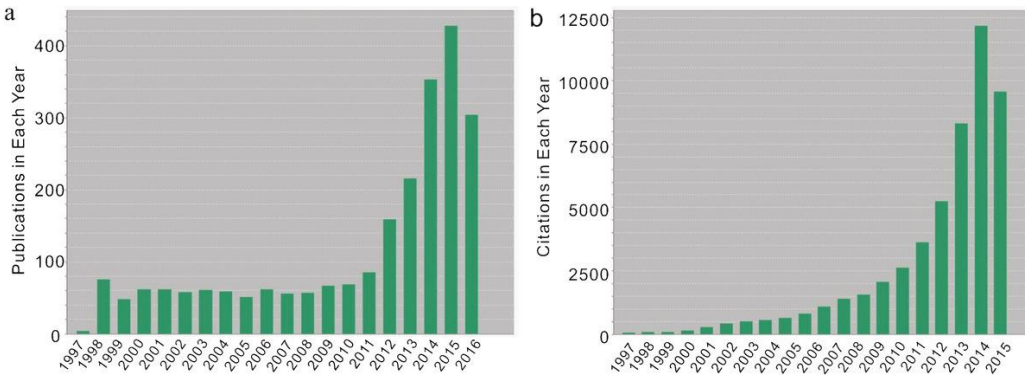

Figure 1.3 The quantity of articles and bibliography on electrochemical CO_2R during the past two decades (Zhang et al., 2017).

According to recent theoretical and experimental findings, metal electrode materials can be classified into four main categories based on the selectivity of the end products: the first category is represented by Pb, Bi, Sn, Cd, Tl and In, which have a low binding energy for the important intermediate *CO and primarily produce formate. (Hori et al., 1994, Huang et al., 2019, Zhang et al., 2017, Zhang et al., 2018b); the second group is represented by Zn, Ag, Zn, Pa and Ga, which have a fierce binding capacity for the key medium *CO and a slightly stronger adsorption capacity for *H, mainly producing carbon monoxide (Birdja et al., 2017, Jiang et al., 2018a, Rosen et al., 2015, Trindell

et al., 2017, Zhang et al., 2018a); the third group is represented by Ni, Fe, Pt and Ti, which have extremely strong C-M bonds, low hydrogen precipitation overpotentials and little reduction of CO_2, with H_2 as the main product (Nitopi et al., 2019); the fourth group is copper, which both inhibits hydrogen precipitation and has a moderate binding energy to intermediates. It provides the conditions for dimerization reactions that can generate numerous C_1, C_2 and C_{2+} products, which are prominent in the production of hydrocarbons, aldehydes and alcohols.

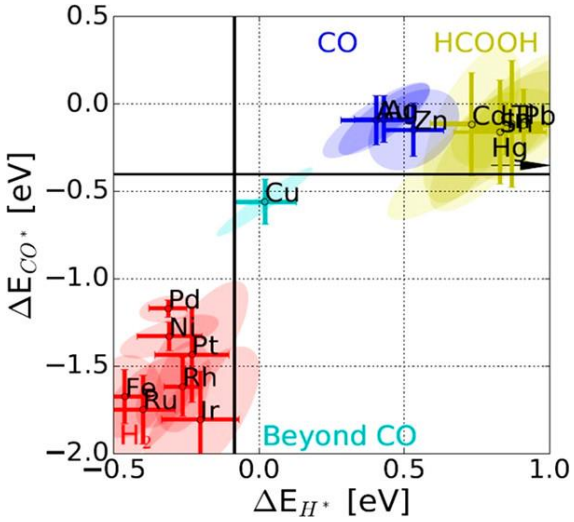

Figure 1.4 CO_2 reduction metal classification (Bagger et al., 2017).

1.2.2 Mechanism on CO_2 Reduction Reaction

The CO_2 molecule has a centrosymmetric linear structure with a C=O bond (length 0.04 Å) smaller than that in ketones, exhibiting triple bond-like properties. And it is thermodynamically inert and therefore chemically very stable, making the transformation of CO_2 into desirable ingredients by electrochemical processes very challenging (Atkins and De Paula, 2002, Greenwood and Earnshaw, 2012). The involvement of a catalyst can shorten the time required to reach equilibrium in electrochemical CO_2 reduction

reactions (CO_2RR), control the selectivity of different products and effectively inhibit the occurrence of hydrogen precipitation reactions (Elgrishi et al., 2018). CO_2RR processes are usually carried out in three steps: the initial procedure is the distribution of CO_2 molecules across the catalysts' surface by chemisorption. The C=O double bond receives high energy electrons and protons in the second step, which causes the double bond to break and the creation of C-O or C-H. The third step is that the products of the reduction reaction are desorbed from the catalyst surface (Duan et al., 2017). Table 1.1 below displays the equilibrium potentials (E°) and electrode reaction equations for the electrochemical CO_2R to multiple products. The electrochemical CO_2R reactions have similar thermodynamic equilibrium potentials to the hydrogen evolution reaction (HER), in accordance with the table. As a result, the CO_2R process in an aqueous electrolyte is accompanied by powerful competing HER side reactions, making the CO_2RR more challenging to occur (Cheng et al., 2019). In particular, with regard to the formation of C_2 and C_{2+} chemical materials, both the thermodynamic energy barrier of CO_2 activation and the thermodynamic energy barrier of C-C coupling need to be overcome. In addition to this, the creation of C-C is kinetically unfavorable compared with the creation of C-H via proton transfer to a C_1 intermediate. And because hydrocarbons and alcohols require more electrons to be transferred, the generation of hydrocarbons and alcohols by electrochemical CO_2R exhibits a greater kinetic potential barrier than the creation of C_1 chemical materials like carbon monoxide and HCOOH and therefore requires a higher overpotential (Liu et al., 2020).

Table 1.1 Some electrochemical reactions that may occur in CO_2R with their equilibrium potentials.

Reaction	E°/ (V vs. RHE)
$2H^+ + 2e^- \rightarrow H_2$	0
$CO_2 + 2H^+ + 2e^- \rightarrow \mathrm{HCOOH}$	-0.12
$CO_2 + 2H^+ + 2e^- \rightarrow \mathrm{CO} + H_2\mathrm{O}$	-0.10
$CO_2 + 6H^+ + 6e^- \rightarrow \mathrm{C}H_3\mathrm{OH} + H_2O$	0.03
$CO_2 + 4H^+ + 4e^- \rightarrow \mathrm{C} + 2H_2O$	0.21
$CO_2 + 8H^+ + 8e^- \rightarrow \mathrm{C}H_4 + 2H_2O$	0.17
$2CO_2 + 2H^+ + 2e^- \rightarrow (\mathrm{COOH})_2$	-0.47
$2CO_2 + 8H^+ + 8e^- \rightarrow \mathrm{C}H_3\mathrm{COOH} + 2H_2O$	0.11
$2CO_2 + 10H^+ + 10e^- \rightarrow \mathrm{C}H_3\mathrm{CHO} + 3H_2O$	0.06
$2CO_2 + 12H^+ + 12e^- \rightarrow C_2H_5\mathrm{OH} + 3H_2O$	0.09
$2CO_2 + 12H^+ + 12e^- \rightarrow C_2H_4 + 4H_2O$	0.08
$2CO_2 + 14H^+ + 14e^- \rightarrow C_2H_6 + 4H_2O$	0.14
$3CO_2 + 16H^+ + 16e^- \rightarrow C_2H_5\mathrm{CHO} + 5H_2O$	0.09
$3CO_2 + 18H^+ + 18e^- \rightarrow C_3H_7\mathrm{OH} + 5H_2O$	0.10

The reaction pathway for electrochemical CO_2R has been described in a variety of ways, as shown in Figure 1.5. In the electrocatalytic CO_2RR, numerous different reaction intermediates are involved, as well as multi-step proton-coupled charge transport stages, C-C coupling processes, and therefore a broad range of products from CO_2R. The relatively easy products to obtain are CO and HCOOH, as they only involve a two-step proton-coupled charge transport process. In the case of HCOOH, there are two possible reaction pathways in the metal catalytic site. The proton-coupled charge transport process forms the $HCOO^-$ intermediate. For the electrochemical CO_2R to CO,

the reaction pathway is generally considered to be that the reactant CO_2 molecule undergoes a proton-coupled charge transport process at the catalytic active site to form the most critical intermediate *COOH, followed by a proton-coupled charge transport process and the removal of an H_2O molecule to form the *CO intermediate. Finally, *CO is removed from the catalytic active site. The final *CO intermediate is then desorbed from the catalytically active site to form CO gas. For other hydrocarbons and multi-carbon products, the ability of multiple *CO intermediates to engage in a C-C coupling process and the strength of *CO intermediate's binding located in the catalytic active center are the determining factors. When the binding strength of *CO located in the catalytic active site is strong, the *CO intermediates are less likely to desorb from the active site and form CO gas for release, but continue to undergo subsequent proton-coupled electron transfer processes at the appropriate potential to form hydrocarbons. For example, a *CO intermediate can go through a further six-step proton-coupled electron transfer process to form methane. When multiple *CO intermediates are not easily detached from the catalytic center then experience C-C coupling processes with each other, the *CO intermediates can turn into different types of reaction intermediates at the appropriate potentials to produce multi-carbon products. The production of ethylene, for instance, can result from the C-C coupling of two *CO intermediates and an eight-step proton-coupled electron transfer process. (Cheng et al., 2015, Hori et al., 1994, Kortlever et al., 2015, Kuhl et al., 2012, Liu et al., 2019, Peterson et al., 2010).

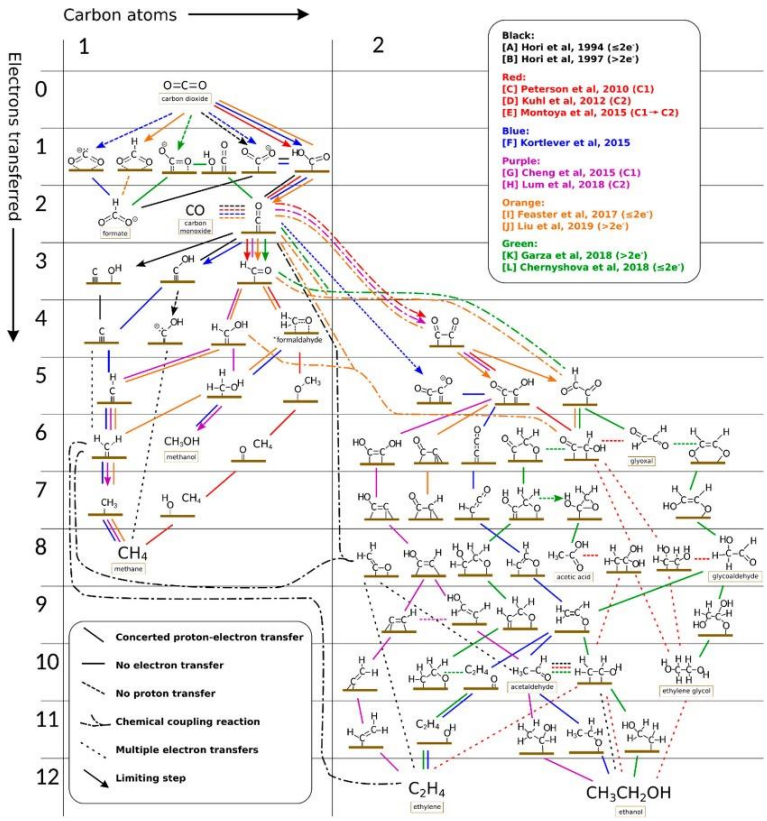

Figure 1.5 Mechanisms on polycrystalline Cu for the transformation of CO_2 into some simple organic substances (Nitopi et al., 2019)

1.3 Research Objectives

Numerous CO_2 reduction techniques and employed catalysts have been reported. However, CO_2 is poorly soluble in water, and the reaction's overpotential is high, particularly when it comes to the production of C_2 products. These troubles make the capacity of CO_2 adsorption upon the catalyst surface more difficult and the competing hydrogen precipitation side reactions are serious, which seriously limit the practical application of electrochemical CO_2R. Due to its moderate adsorption energy for CO_2 activation intermediates, copper metal is currently the sole metal catalyst capable of electrochemical CO_2R towards high energy density C_2 and C_{2+} products. Despite the excellent

electrocatalytic reduction performance of copper metal for CO_2, it still suffers from complex reduction products, low single product selectivity and poor stability. Because of this, the practical application of electrochemical CO_2R greatly benefits from the rational design of copper catalysts to enhance CO_2 transformation and the selectivity of desired products, particularly the selectivity of C_2 and C_{2+} products like C_2H_4 and C_2H_5OH at low potential and high current density.

Graphitic phase carbon nitride (g-C_3N_4) frameworks containing specific N atoms with strong ability to give electron in triazine/heptazine heterorings have been reported, to serve as molecular brackets for the proper design of the electronic structure of the metal element to bring outstanding electrochemical activity in CO_2RR (Zheng et al., 2017, Zou et al., 2013). In this study, starting from structure of the catalytic material of electroreduction, g-C_3N_4-supported CuO catalysts was formed based on copper oxide catalysts using g-C_3N_4 as a carrier by a straightforward hydrothermal method combined with calcination (recorded as CuO/g-C_3N_4). The morphology and structure were analyzed by XRD, FTIR, SEM, HRTEM, XPS and other characterization methods. The electrochemical performance and catalytic activity of the material as a cathode material were investigated by drop coating the catalysts on carbon paper using LSV, EIS and other test methods, and the performance of the electrochemical CO_2R yielding different products at various potentials was tested mainly using chronopotentiometry (CP). During the results, the reasons for the efficient catalytic reduction to C_2 by CuO/g-C_3N_4 electrode were comprehensively analyzed.

1.4 Structure of Chapters

Copper-based catalysts have experienced extensive research in the sector of electrochemical CO_2R, and in recent decades, as the mechanism of electrochemical CO_2R to different products has become clearer, various pathways have been developed along different directions to improve the single product selectivity and multi-carbon product efficiency of conventional metallic copper catalysts. In Chapter II, some typical reaction paths of C_2 products were discussed, and four main types of current copper-based catalysts for the deep CO_2R to C_2 and C_{2+} products were reviewed, including: optimization of the copper crystalline surface, alloying copper with a second metal, etc., with a focus on the analysis of modulating the valence state of copper and the construction of oxygen defects through more synergistic active sites as well as electronic effects and geometric effects to influence the reactivity. Besides, the structure, properties, and synthesis methods of g-C_3N_4 have been fully explored, but the existing studies are still very limited, especially the effects of introducing metal elements in the molecular structure of g-C_3N_4 on the catalytic and electrochemical characteristics. Therefore, in the following Chapter III, CuO-loaded g-C_3N_4 structured electrocatalysts were innovatively designed, and materials, synthesis methods, as well as the characterization and testing methods were described in detail. The characterization results and the large amount of data obtained from electrochemical tests were analyzed one by one in Chapters IV and V, respectively, and the comparison arguments with commercial CuO and laboratory-produced pure CuO were used to explain from different

perspectives. This creates the groundwork for future high performance and adaptable catalyst synthesis as well as for a better comprehension of the catalytic mechanism. Further, a summary and outlook of the whole work was given in Chapter VI.

CHAPTER II. LITERATURE REVIEW

2.1 Copper-based Catalysts for CO_2 Deep Reduction Reactions

Copper has moderate *CO adsorption energy, and under the action of suitable electric potential, metallic copper can reduce CO_2 to as many as 16 C_1 ~ C_3 products, showing great capacity for deep CO_2R. However, the CO_2 deep reduction activity of common copper catalysts is low. CO_2R products are mainly hydrogen and carbon monoxide, and the C_2 products obtained from other deep reductions are less selective, which is difficult to meet the expectation of transforming CO_2 into higher value-added products. In order to promote the reactivity of Cu-based catalysts for deep CO_2 reduction to enhance in more depth the capacity of C_2 and C_{2+} products, researchers have carried out a series of modification and improvement works on them in the past from various aspects such as morphology control, electronic structure control, and valence control (Bagger et al., 2017, Kuhl et al., 2012).

2.1.1 Copper Metal Catalysts

Metallic copper catalysts have the potential for deep CO_2 reduction. However, conventional metallic copper electrodes, such as copper flakes and copper pellets, require a large overpotential (>1 V vs. RHE) to achieve the transformation of CO_2 to C_2 products (Feng et al., 2016). Concerning increasing the deep CO_2 reduction reactivity of metallic copper catalysts, the conformational relationship between metallic copper and deep CO_2 reduction activity needs to be further clarified. But conventional polycrystalline copper

has several different crystalline surfaces with complex surface structures, which is not conducive to explore how specific crystalline surfaces affect the selectivity of C_2 products. Hori et al. methodically studied the CO_2R activity of single-crystal Cu with different crystalline surfaces and found that Cu(111) favored the production of CH_4, while another crystalline surface Cu(100) preferred the production of C_2H_4, and Cu(110) contribute to the direction of CH_3COOH (Hori et al., 2003). Schouten et al. monitored more clearly the product distribution of single-crystal Cu on different crystalline planes by online electrochemical mass spectrometry, and their experimental results demonstrate that two reaction pathways may exist on Cu (Schouten et al., 2012). The tetragonally arranged Cu atom arrays are important reaction sites for CO-CO, and they stabilize the electronic and kinetic equilibria of the C-C coupling intermediates, making Cu(100) more supportive for the generation of C_2 products (Li et al., 2014b). In addition to this property, Cu(100) possesses a lower C-C coupling activation energy than Cu(111) in DFT calculations due to the evidence that (100) plane is more favorable for the capture of the key intermediate *CO compared to Cu(111), thus exhibiting a higher *CO covering rate (Montoya et al., 2015, Sandberg et al., 2016). Thus, for pure metallic copper catalyst, Cu(100) crystalline facets are more favorable than Cu(111) crystalline facets to facilitate the transformation of carbon dioxide to dicarbon products.

Based on the variability of reactivity of different crystalline facets of metallic copper, tuning the exposed crystalline facets of metallic copper is a reliable method to enhance the selectivity of C_2 and C_{2+} products. Jiang et al. formed

cubic metallic copper with exposed Cu(100) facets on copper sheets by cyclic deposition dissolution of metal ions. The experimental results show that the metallic copper catalyst with exposed (100) facets has more than twofold improvement in C_2 products selectivity over the original copper sheets (Jiang et al., 2018b). Similarly, Wang et al. found that the passage of CO_2 during electrodeposition effectively enhanced the proportion of exposed Cu(100) facets in metallic Cu catalysts, thereby increasing the Faradaic efficiency of C_2 and C_{2+} products, like C_2H_4 to nearly 90 % (Wang et al., 2020b). The enthalpy change and activation energy of CO dimerization on Cu(100) are lower than those of both (111) and (211) facets. Based on the calculation of the adsorption energies by three intermediates, CO_2*, COOH*, and CO*, it revealed that Cu(100) is more favorable for intermediate adsorption and increases with the presence of these intermediates.

In addition to crystal plane control, modulating the nanomorphology of copper metal catalysts can also control the catalyst surface structure in order to change the electrochemical CO_2R activity of the catalysts. Reske et al. synthesized six different sizes of copper metal nanospheres ranging from two nanometers to fifteen nanometers to explore the effect of copper metal size on the CO_2 reduction activity. It was found that smaller size copper particles possessed more low coordination sites, and these sites had a stronger adsorption capacity for intermediates, resulting in weaker CO_2 deep reduction for smaller size copper particles (Reske et al., 2014). The authors constructed a model of copper nanoparticles with non-faceted surfaces. For small particle sizes, undercoordination was observed for specific coordination numbers less than 8.

The sharp increase in atoms with strong binding sites accelerates the formation of CO but reduces the mobility of CO and H intermediate species. For large particle size catalyst particles, the weaker binding of CO and H favors the formation of hydrocarbons. On the other hand, Loiudice et al. tuned the size of cubic copper metal nanoparticles and found that among the 63 nm, 44 nm and 24 nm cubic copper, the 44 nm cubic copper catalyst exhibited the highest ethylene activity with a Faradaic efficiency of 41 %. In this regard, they suggested that the largest proportion of boundary sites of 44 nm metallic copper to various surface sites was responsible for the superior catalytic activity of C_2 products exhibited by cubes of this size (Loiudice et al., 2016). Li et al. found that the regular metallic copper nanowire morphology was initially at -1.25 V vs. RHE due to the abundance of twinned boundary sites, so that the reduction products were mainly dominated by methane (about 50 %), but as the electrochemical CO_2RR proceeded, the copper nanowire morphology changed, resulting in a steadily rise in the Faradaic efficiency of ethylene (Li et al., 2017). In addition, Jeon et al. also prepared prism-shaped metallic copper catalysts by electrodeposition. This special morphology allows the catalyst surface to have more defects and unsaturated coordination sites, which improved the Faradaic efficiency of ethylene (Jeon et al., 2018). From these above research works, it can be found that these copper catalysts with different nanomorphologies cause different exposed crystalline surfaces or reaction sites of metallic copper, which changes the products' dispersion of CO_2 electroreduction.

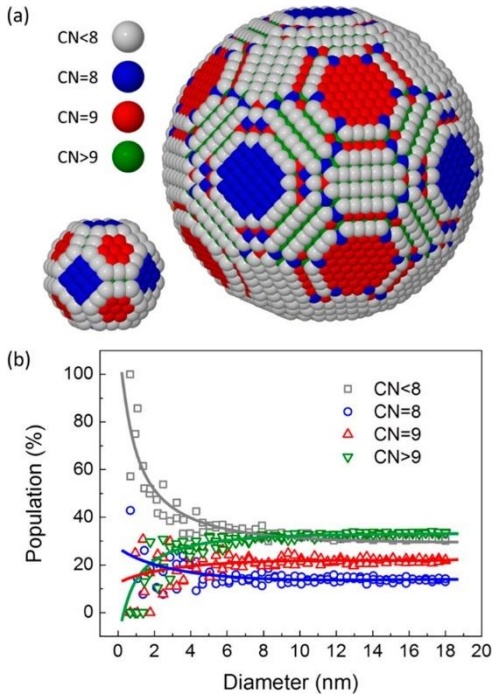

Figure 2.1 (a) Ball models of copper nanoparticles with different diameters. (b) Number of surface atoms as a function of diameter with a given coordination population (Reske et al., 2014).

Although nanomorphology modulation of copper catalysts can make the selectivity of C_2 products improved, whether the nanocatalyst morphology can be maintained during the reaction is an important issue to be concerned about. Kley et al. discovered the selectivity of overall C_2 products reduction exhibited by the catalysts gradually increased as the amount of copper particle catalysts loaded on carbon paper increased. It was observed by SEM that the copper particles agglomerated together after a period of reaction and formed cubic morphologies of varying sizes, thus confirming the phenomenon that copper nanoparticles undergo morphological changes even at lower reaction potentials (Kim et al., 2017). It is such morphological changes that lead to further enhancement of Faradaic efficiencies of C_2 products such as ethylene and

ethanol. Therefore, when studying the effect of nanomorphology of copper-based catalysts on electrochemical CO_2R activity, researchers should focus on the changes of the studied copper-based catalysts before and after the electrochemical CO_2RR.

2.1.2 Copper-based Bimetallic Catalysts

Copper has a moderate adsorption energy for various intermediates of the CO_2RR, resulting in a low selectivity for various products. The introduction of a second reactive site with different adsorption energy can modulate the adsorption energy of the copper-based catalysts surface for the intermediate species, thus enabling the change of reaction pathway. This modulating effect on electrochemical CO_2R activity and selectivity can be put down to the addition of a second metal that modifies the geometric and electronic structure of the copper atoms. When the second metal is embedded in the lattice of copper atoms it causes a transformation in the original interatomic spacing between surface atoms, changing the electron d-band centers, and thus the binding strength related to the intermediates of the reaction (Lee et al., 2018). Based on the different affinities of H and O, various metals can be categorized into four categories to directing the design of copper-based alloy catalysts, using copper as a reference (Bagger et al., 2017).

The first group of metals, represented by Au and Ag, has a stronger oxygenophilic capacity and a weaker hydrogenophilic capacity than Cu, with a weaker adsorption capacity for CO. Thus, in the electrochemical CO_2RR, CO in the adsorbed state will rapidly desorb from the surface of such metals and

form CO (Chen et al., 2012, Daiyan et al., 2017, Feng et al., 2015, Zhao et al., 2018a). When Au and Cu form an alloy, the Faradaic efficiency for CO of the CuAu alloy is significantly improved over that of a single Au or Cu metal catalyst, but this improved performance cannot be attributed solely to the electronic or morphological interaction between gold and copper (Kim et al., 2014). Hoang et al. synthesized CuAg alloy nanowires containing 6 % Ag and found that this fully phase mixed AgCu alloy was found to achieve 60 % and 25 % Faradaic efficiency for ethylene and ethanol respectively, which is the highest level among copper-based alloy catalysts so far (Hoang et al., 2018). The second group of metals such as Sn and In have a strong adsorption capacity for O and a weak affinity for H. Therefore, the *COOH generated on the surface is rapidly shed to form formic acid (Xia et al., 2018, Gu et al., 2018). However, the *CO intermediate in the CuSn bimetallic system, is theoretically unaffected by the O binding site. The CuSn alloy catalyst synthesized by Sarfraz et al. with Sn modified Cu surface has a high CO Faradaic efficiency of 95 % in the electrochemical CO_2RR (Sarfraz et al., 2016). Pd has a strong hydrogen adsorption capacity and can form stable Pd-H bonds. Therefore, the involvement of Pd in the CuPd system can be more favorable for the formation of *COH or *CHO by protonation of the adsorbed state *CO. However, Li et al. concluded by DFT calculations that Pd is the main site in the CuPd alloy and the electronic interaction between CuPd facilitates the conversion of CO_2 to CO, thus enabling the CuPd alloy to obtain higher than 80% CO Faradaic efficiency (Li et al., 2016b). Further, Kenis et al. investigated the electrochemical CO_2R performance of CuPd catalysts with different mixing modes and found that in phase separated CuPd. The C_2

products Faradaic efficiency could reach 60 %, while other mixed-mode CuPd had almost no C_2 products activity (Ma et al., 2017). This work suggests that the electronic interaction between the alloys is not a primarily dependent in improving the C_2 products selectivity of the catalysts.

With the exception of the alloying effect of the bimetal, a second metal can be used as a co-catalyst to improve the C_2 and C_{2+} product selectivity by providing a *CO intermediate to the copper catalyst. Ager et al. effectively improved the Faradaic efficiency for ethanol of Au/Cu catalysts (41.4 %) by constructing regular Au arrays on copper sheets, and the Au catalyst coverage on copper could be further adjusted to regulate the products. Yeo's group reported a higher ethanol product selectivity (~29 %) for CuZn catalysts than for copper catalysts undoped with Zn atoms (Ren et al., 2016). In situ Raman spectroscopy showed that *CO had adsorption behavior only at the Cu atomic sites of the CuZn catalysts. Based on the experimental results, they concluded that *CO was generated at the Zn atomic sites and then transferred to the neighboring Cu atomic sites for subsequent deep reduction reactions, coupled with $*CH_2$ adsorbed on the Cu sites to form $*COCH_2$, and finally reacted to produce ethanol. A similar phenomenon exists in the Ag-Cu system. Lee et al. found that Cu_2O mixed with Ag atoms has a three-fold height Faradaic efficiency for ethanol than that of pure Cu_2O (Li et al., 2017), owing to the presence of abundant boundary sites between Ag and Cu_2O which facilitates the migration of CO to the Cu sites. Further, Jaramillo et al. found that physical deposition of Au particles on Cu reduced the overpotential of alcohol products and elaborated mechanism of tandem catalysts between Au and Cu by

analyzing the CO consumption. When a second metal site with high selectivity for CO is doped on Cu, the CO generated on the second metal site can overflow onto Cu, thus increasing the *CO coverage on Cu and more favorable for the C-C coupling reaction (Lum and Ager, 2018a). Using this strategy of tandem catalysts can effectively improve the selectivity of C_2 and C_{2+} products for copper catalysts.

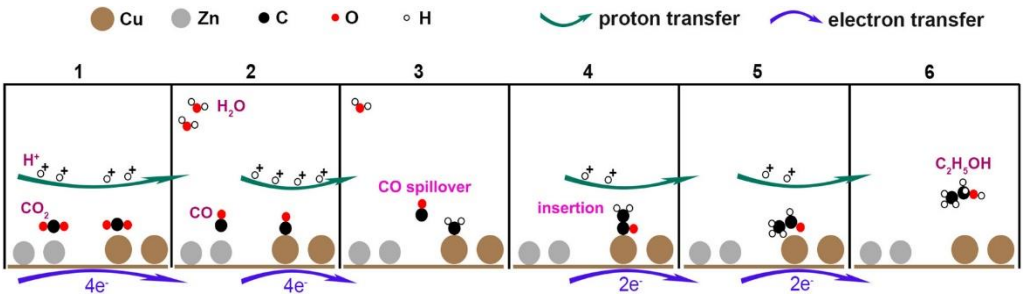

Figure 2.2 Proposed mechanism for CO_2 to ethanol on Cu_xZn electrocatalysts.(Ren et al., 2016)

2.1.3 Oxide-derived Copper Catalysts

Copper oxides are not stable under electrochemical CO_2R conditions and are rapidly reduced to oxide-derived copper (OD-Cu). OD-Cu formed by electroreduction is able to limit CO and CO_2 to higher value multi-carbon products. Kanan et al. performed a carbon monoxide reduction study on their oxide-derived Cu foil (Li et al., 2014a). OD-Cu exhibits high selectivity for liquid phase products such as ethanol and acetate between -0.25 and -0.40 V vs. RHE, with an appreciable ethanol yield of 43% at -0.3 V vs. RHE. OD-Cu derived from Cu_2O also exhibited superior Faradaic efficiency for C_2 products in electrochemical CO_2R, which could reach 42.6 % for ethylene at -31.2 $mA \cdot cm^{-2}$ (Handoko et al., 2016). It has been shown that OD-Cu generally has higher CO_2 deep reduction activity than ordinary copper catalysts in CO_2 deep

reduction (Ke et al., 2017, Lum et al., 2017). The reason for this improved performance has also attracted the attention and consideration of researchers.

During the rapid reduction of copper oxides, the rapid stripping of oxygen atoms causes a dramatic alteration in the surface characteristics of OD-Cu. The surface structure of different morphologies of copper oxide or cuprous oxide are changed under electrocatalytic CO_2R conditions (Mandal et al., 2018). This change in morphology results in a rougher surface of OD-Cu catalysts and its electrochemical active surface area (ECSA) enhanced (Hori et al., 1997). Under the induction of carbon monoxide, the surface of OD-Cu obtained by electroreduction undergoes a drastic remodeling, and its surface becomes rich in coordination-unsaturated copper nanoparticles. These ligand-unsaturated sites have stronger *CO adsorption capacity, which effectively improves the selectivity of CO to n-propanol. Jung et al. synthesized Cu_2O nanoparticles and found that after electrochemical CO_2R, Cu_2O fragmented into numerous 2 ~ 4 nm OD-Cu particles (Jung et al., 2019). This drastic change in morphology promotes the output of C_2 products while inhibiting the HER reaction, leading to a Faradaic efficiency of 57.3 % for ethylene and 74.0 % for C_2 products. However, it is difficult to quantify the performance changes due to such morphological changes. However, on the other hand, Klinkova et al. documented the process in detail and inferred mechanism of morphology change of copper hydroxide cubes under electroreduction conditions, and found that although the morphology of copper catalysts at different stages were different, their CO_2 reduction performance and product distribution were similar. So it was suggested in the paper that morphology change of OD-Cu

catalysts might not be the key reason for promoting deep CO_2R (Basiratnia et al., 2019).

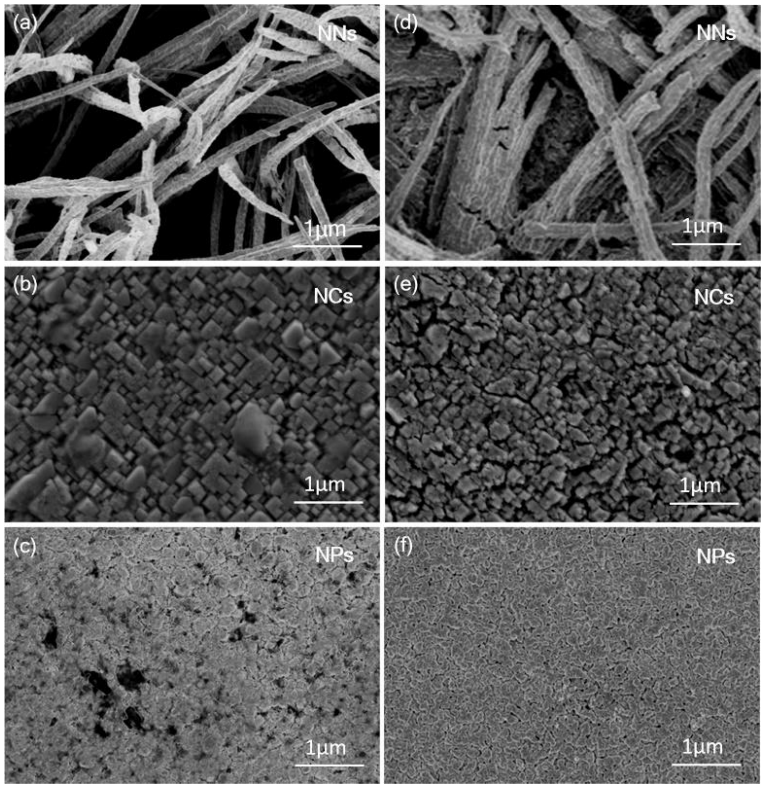

Figure 2.3 SEM images of copper oxides before CO_2R (a, b, c) and after CO_2R (d, e, f) (Mandal et al., 2018).

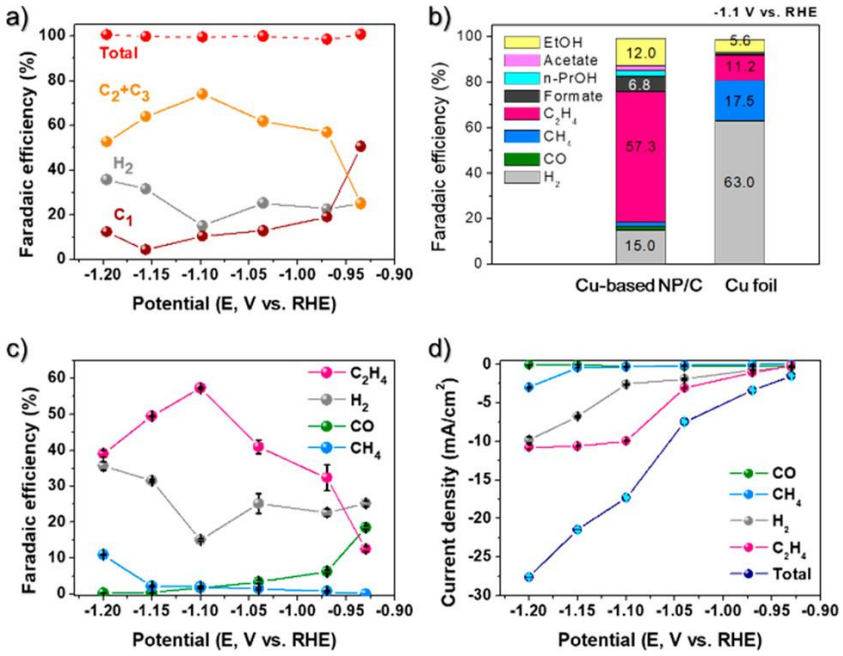

Figure 2.4 NP/Carbon based on fragmented Copper exhibits electrochemical CO_2RR performances: a) Faradaic efficiencies classified by H_2 and C_1 ~ C_3 at -0.9 ~ -1.2V vs. RHE, b) accumulation of bars showing the quantity of products at -1.1 V vs. RHE in comparison to copper foil, Faradaic efficiencies c) and (total) partial current densities d) for: H_2, CO, CH_4 and C_2H_4 (Basiratnia et al., 2019).

The reduction from copper oxide to OD-Cu involves a change in the oxidation state of Cu. Therefore, the change of Cu oxidation state is also considered as one of the possible factors for the higher selectivity for C_2 and C_{2+} products of OD-Cu. However, the issue of the oxidation state of Cu in the electrochemical CO_2R process has been a still controversial issue. In situ X-ray absorption spectroscopy has shown that Cu^+ can be present in the catalysts under CO_2RR conditions and can promote ethylene production (De Luna et al., 2018). Mistry et al. oxidized Cu to CuO by oxygen ion activation and found that the Faradaic efficiency for ethylene of OD-Cu obtained by this method could reach 60%.

Associated with in situ X-ray absorption spectroscopy results, there are Cu^{+} on the surface of the catalysts (Mistry et al., 2016). Many subsequent works have similarly concluded that the presence of Cu^{+} can lead to higher C_2 and C_{2+} yielding activity of copper catalysts (Daiyan et al., 2019, Kim et al., 2019). At the theoretical computational level, Xiao et al. demonstrated that the division of labor between Cu^{0} and Cu^{+} on the layer of copper catalysts is what fosters the activation reducing CO_2 molecular and promotes C-C coupling by modeling the catalyst of copper in metallic state embedded in copper oxide (Xiao et al., 2017). However, on the other hand, with the development of in situ characterization techniques and isotope experiments, more and more experiments have demonstrated that Cu^{+} is difficult to stabilize under electrocatalytic conditions. By labeling the oxygen atoms in copper oxide with isotope experiments, Ager et al. found that the remaining amount of ^{18}O in the OD-Cu after the reaction was less than 1 % of the starting amount, fully indicating that all the oxygen of copper oxide would be stripped by reduction under the reaction conditions and no oxide state would exist (Lum and Ager, 2018b). Cuenya et al. combined in situ XAS and quasi-in situ XPS and other characterization means, demonstrated that OD-Cu is free of Cu^{+} in the reacted state. The excellent C-C coupling activity does not come from the presence of CuO_x. In situ X-ray diffraction spectroscopy (XRD) also demonstrated that OD-Cu is not present in the oxidation state of Cu in the reacted state (Scholten et al., 2019). This shows that Cu is a very oxidizable metal and the discrimination of its valence state in the reaction should be based on in situ characterization tools. With the advancement of in situ characterization means, the issue of the valence state of Cu in OD-Cu will become clearer.

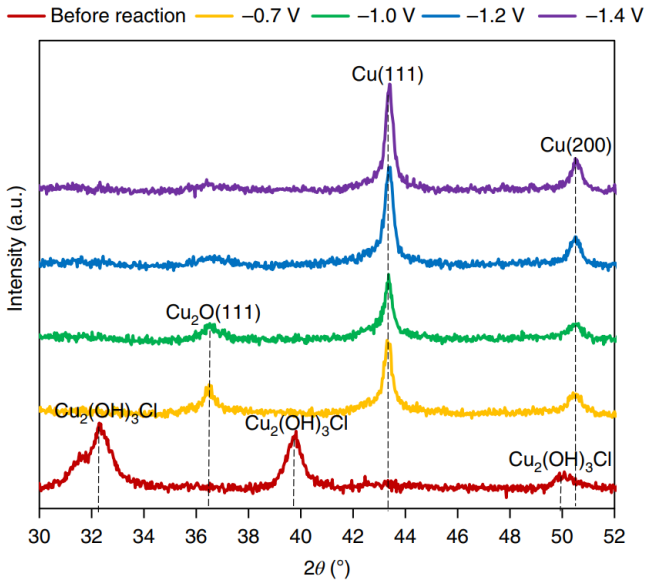

Figure 2.5 A comparison of the ERD Cu before- and after-reaction XRD patterns at various applied potentials (De Luna et al., 2018).

Table 2.1 Summary of electrocatalytic reduction of CO_2 to selective C_2 products.

Electrode	Preparation method	Electrode potential or current density	Electrolyte	Products and Faradaic efficiency (%)	Ref.
Cu foil	Potentiostatical electropolish	-1.05 V vs. RHE	0.1 M $KHCO_3$	C_2H_4 (<25%) C_2H_5OH (10%)	(Kuhl et al., 2012)
Cu(100)	Electrochemical polish	5 mA cm^{-2}	0.1 M $KHCO_3$	C_2H_4 (40.4%) C_2H_5OH (9.7%)	(Hori et al., 2003)
Cu nanocube	Metal ion battery cycling method	>40 mA cm^{-2}	0.25 M $KHCO_3$	C_2 (>60%)	(Jiang et al., 2018b)
Cu(100) nanocube	In situ electrodeposition	-0.49 V vs. RHE	7 M KOH	C_2 (90%)	(Wang et al., 2020b)
Cu NP	Inverse micelle encapsulation	-1.10 V vs. RHE	0.1 M $KHCO_3$	C_2H_4 (20%)	(Reske et al., 2014)
Cu cubes with 44 nm edge length	Colloidal chemistry	-1.10 V vs. RHE	0.1 M $KHCO_3$	C_2H_4 (41%)	(Loiudice et al., 2016)
Prism-shaped Cu	One-step electrodeposition	-1.10 V vs. RHE	0.1 M $KHCO_3$	C_2H_4 (27.8%)	(Jeon et al., 2018)
Cu NPs	Reduction of copper	-0.75 V vs. RHE	0.1 M	C_2-C_3 (50%)	(Kim et

	(I) acetate (CuAc) precursor		$KHCO_3$		al., 2017)
CuAg alloy films	Electrodeposition	-0.70 V vs. RHE	0.1 M $KHCO_3$	C_2H_4 (60%) C_2H_5OH (25%)	(Hoang et al., 2018)
Phase-separated CuPd	Liquid phase reduction	-0.80 V vs. RHE	1 M KOH	C_2 (63%)	(Ma et al., 2017)
Oxide-derived Cu4Zn	Galvanostatically depositon	-1.05 V vs. RHE	0.1 M $KHCO_3$	C_2H_5OH (29.1%)	(Ren et al., 2016)
Ag-Cu core-shell	One-step reduction	-1.06 V vs. RHE	0.1 M $KHCO_3$	C_2H_4 (18%) C_2H_5OH (25%)	(Lee et al., 2017)
AuCu	Electrodeposition	-1.00 V vs. RHE	0.1 M $KHCO_3$	C_2-C_3 (65%)	(Lum and Ager, 2018a)
Cu_2O-derived Cu	Hydrothermal method	31.2 mA cm^{-2}	0.1 M $KHCO_3$	C_2 (42.6%)	(Handoko et al., 2016)
CuO-derived porous Cu NRAs	Electrochemical reduction	-0.70 V vs. RHE	0.1 M $KHCO_3$	C_2H_4 (23%) C_2H_5OH (13.7%)	(Ke et al., 2017)
EC Cu	Electrochemical oxidation-reduction cycling	-1.00 V vs. RHE	0.1 M $CsHCO_3$	C_2 (70%)	(Lum et al., 2017)
Cu-based NP/C	One-pot, wet-chemical synthesis	-1.10 V vs. RHE	0.1 M $KHCO_3$	C_2H_4 (57.3%) C_2 (74.0%)	(Jung et al., 2019)
ERD Cu	Electro-redeposition	-1.00 V vs. RHE	0.1 M $KHCO_3$	C_2H_4 (38%) C_2 (52%)	(De Luna et al., 2018)
Plasma-activated Cu	O_2 and H_2 plasmas	-1.00 V vs. RHE	0.1 M $KHCO_3$	C_2H_4 (60%)	(Mistry et al., 2016)
Branched CuO nanoparticles	Polyol process	-1.00 V vs. RHE	0.1 M $KHCO_3$	C_2H_4 (70%)	(Kim et al., 2019)
Cu_xO/Ag	O_2 plasma	-0.70 V vs. RHE	0.1 M $KHCO_3$	C_2-C_3 (>40%)	(Scholten et al., 2019)

2.2 Overview of g-C_3N_4

C_3N_4 is one of the oldest man-made polymers, and its precursors can date back to the 19 century, when Liebig and Berzelius first synthesized a linear polymer

of trisulfotriazine and called the molecule "melon", marking the dawn of the graphitic phase of carbon nitride. Redemann and Lucas proposed that melon was a derivative formed by mixing polymers of different sizes and structures (Redemann and Lucas, 1940). However, melon-based C_3N_4 was gradually forgotten due to its inactive chemistry and insolubility in most solvents until Liu et al. predicted the existence of β-C_3N_4 with hardness comparable to diamond by theoretical calculations and measured its C-N bond length to be 0.147 nm (Liu and Cohen, 1989). Since then, the research on C_3N_4 has been resumed. In the 1990s, Hemley et al. reworked the theoretical study of C_3N_4 and proposed the following five possible crystal structure models for C_3N_4 materials: β-C_3N_4, α-C_3N_4, c-C_3N_4 (cubic phase), p-C_3N_4 (quasi cubic phase) and g-C_3N_4 (graphite-like phase) (Teter and Hemley, 1996). Among them, g-C_3N_4 at present has already been broadly applied in the area of multiphase catalysis because of its abundant source of raw materials, simple synthesis method, and special electrical properties and electronic structure.

2.2.1 Structure and Properties of g-C_3N_4

g-C_3N_4 is the only soft phase among the whole carbon nitride materials and has the highest thermal and chemical stability at room temperature. In 2008, Wang et al. found that g-C_3N_4 molecule consists of two types of structural unit, s-triazine ring (C_3N_3) and 3-s-triazine ring (C_6N_7) (Wang et al., 2009). The stability of g-C_3N_4 is constrained by the various electronic surroundings of the nitrogen elements of the two structural units, and the different periodic arrangements of the basic structural units within their own layers lead to the formation of nitrogen pores with different shapes and different sizes. The

carbon and nitrogen atoms of both basic units undergo sp^2 hybridization and form a conjugated π-bond through the lone pair of electrons to form a hexagonal structure with σ-bonds, which are eventually connected by nitrogen atoms to form an infinitely extended g-C_3N_4 two dimensional organic plane (Cui et al., 2012, Zhang et al., 2010). Kroke et al. showed that the binding energy of g-C_3N_4 with 3-s-triazine ring as the fundamental component is about 30 kJ mol^{-1} less than that of g-C_3N_4 with s-triazine ring as the fundamental component, indicating that the 3-s-triazine ring is more stable (Kroke et al., 2002). In addition, the presence of numerous periodic cavities in the structure of the 3-s-triazine ring unit is conducive to elemental doping and adsorption modifications, making this kind of g-C_3N_4 a focus of research.

g-C_3N_4 possesses a structure close to graphene: two dimensional lamellar, with each layer formed by C-N covalent bonding of atomic layers, and the different layers are bound to each other by van der Waals forces to form a stacked lamellar structure (Huang et al., 2014). The three main types of bonding between different layers are ABCABC type, ABAB type and AAA type with C-C bond length of 0.138 nm and layer spacing of 0.32 nm (Goglio et al., 2008). This layered structure makes g-C_3N_4 chemically and thermally stable. Therefore, g-C_3N_4 is insoluble in most solvents, such as: water, ethanol, acetone, N-dimethylformamide, tetrahydrofuran, ether, and toluene, and is even stable at room temperature under strong acidic and alkaline conditions at pH = 1 or 14. The literature shows that g-C_3N_4 is stable in air at temperatures up to 600 °C, and decomposition starts only when the temperature rises to

630 °C and continues to 700 °C, due to its aromatic C-N heterocycle (Gillan, 2000, Wang et al., 2012).

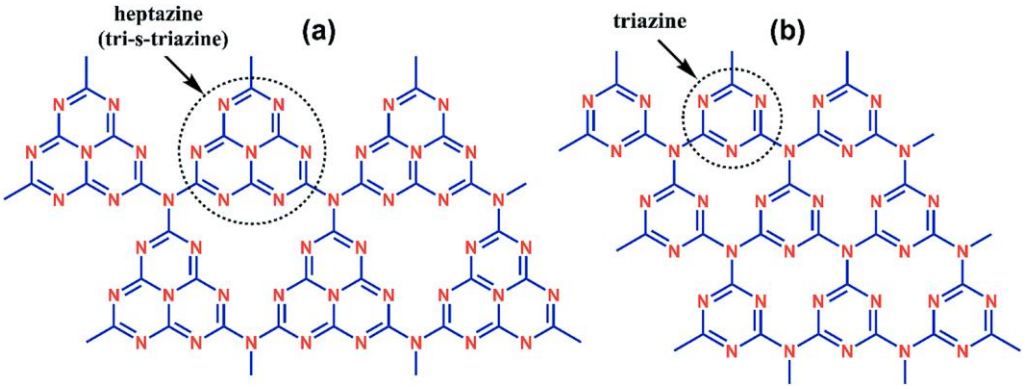

Figure 2.6 Structure of graphitic carbon nitride based on s-heptazine and s-triazine units (Kumar et al., 2018).

2.2.2 Preparation Methods of g-C_3N_4

The current synthesis methods of g-C_3N_4 can be broadly classified into 2 types: physical and chemical methods. The physical methods primarily include high-pressure pyrolysis, ion implantation and mechanical ball milling, which were gradually developed in the process of exploring hard-phase C_3N_4 semiconductor materials. Most of the materials synthesized by these methods are amorphous g-C_3N_4 thin film structures, where the nitrogen content is very low, and the experimental conditions are very demanding. Among the chemical methods, solid-phase reaction and solvothermal methods were the first to be proposed, and later on, thermal polycondensation, supramolecular self-assembly, and templating methods gradually emerged, with thermal polycondensation being the most commonly used method at present (Wang et al., 2020a).

The thermal polycondensation method, as one of the most commonly used preparation processes, uses thermally induced polycondensation of N-rich precursors (for example: dicyanamide, melamine, monocyanamide, urea and thiourea) in air or inert gas atmosphere to transform into melamine dimers and polymerized molecules during the thermal polycondensation process, and finally release NH_3 to transform into g-C_3N_4. As higher heating temperature, the carbonation of g-C_3N_4 increases, the defects increase, and the content of the corresponding N atoms decreases, which is caused by the incomplete condensation of the amine (Yan et al., 2009). It is noteworthy that the presence of defects facilitates the modulation of the electronic structure of g-C_3N_4 and effectively enhances the electrocatalytic activity of its composites.

Supramolecular self-assembly is a method to prepare g-C_3N_4 by non-covalent bonding interactions under equilibrium conditions using organic precursors rich in triazine structures as raw materials. Because of the directionality and specificity of the triazine structure, hydrogen bonding is one of the non-covalent bonding interactions that are most crucial for organizing the supramolecular precursor structure. Although this supramolecular pre-assembly method can improve the structural ordering of g-C_3N_4, it is also influenced by factors such as solvent type, pre-assembly time, calcination temperature and time (Jun et al., 2013).

In terms of template method, the large specific surface area and the abundant mesoporous structure can effectively increase the mass/charge transport rate of g-C_3N_4, thus significantly enhancing its electrocatalytic performance.

Therefore, it is advantageous to adjust the size, morphology and pore structure of g-C_3N_4 using organic or inorganic templates. In general, the structural and morphological characteristics of the synthesized samples are directly related to the template, no chemical reaction should occur between the template and the sample, and the template should be easily removable (Ong et al., 2016).

2.2.3 g-C_3N_4-supported Metal Catalysts for Efficient CO_2 Reduction

For many years, g-C_3N_4 has become a gifted catalyst for photocatalysis due to its better photochemical stability, cost-effective preparation, proper electronic energy band structure and environmental friendliness. As a metal-free material, it has a 2.7 eV band gap, a 1.4 eV valence band, and a conduction band (-1.3 eV), which allows g-C_3N_4 to capture part of the light wave. Despite the good photo response to light wave, the low carrier mobility of pristine two-dimensional nanosheets and the swift complexation of electron-hole pairs generated by photoexcitation are not conducive to the great act of g-C_3N_4. Some improved methods have been explored, including the construction of heterojunctions, optimization of morphology and structure, doping of elements, deposition of noble metals, and modification of quantum dots, to transform pristine g-C_3N_4 and strengthen its activity in photocatalysis (Liu et al., 2021, Zhang et al., 2020, Han et al., 2021).

g-C_3N_4 contains a large amount of pyridine N. As the main active site for electrochemical reactions, pyridine N as a substrate not only stabilizes the metal nanoparticles in a neutral state but also provides an active center for

CO_2R (Zhao et al., 2018b). Inspired by these, metal (metal oxide)-C_3N_4 binary electrocatalysts using various metals and their oxides as modules were developed.

Zhang et al. found that g-C_3N_4-loaded Au particles (Au/C_3N_4) performed better performance for CO_2R than C-loaded Au particles (Au/C). Au/C_3N_4 not only revealed much higher CO partition current than Au/C at all studied voltages, but also showed a CO selectivity is over 90 percent at an overpotential of -0.45 V vs. RHE. Theoretical calculations indicate that the contact of C_3N_4 with Au results in a highly electron-rich surface of Au, which enhances the adsorption of the crucial kinetic intermediate *COOH. Meanwhile, they used the same method to load Ag nanoparticles on C_3N_4 (Ag/C_3N_4), and XPS results showed that Ag nanoparticles also have an electron-rich surface (Zhang et al., 2018a). Fu et al. studied multiple C-C coupling routes on various combinations of copper with carbon/nitrogen active catalysis sites using DFT calculations on copper with C_3N_4 and the C_2H_4 production. Mechanism of the reaction of C_2H_4 production was investigated in depth. When CO_2 molecules are reduced to intermediates such as *CO, *CHO, and *COOH on Cu, the carbon atoms in g-C_3N_4 provide a sink site for the intermediates on the Cu sites, and this transfer of active centers indicates the synergistic effect of C and Cu. Moreover, C shows a great affinity for O-containing reaction intermediates, which facilitates further reduction of intermediates to obtain C_2 products during CO_2RR (Fu et al., 2021). This demonstrates that efficient production of CO_2 to C_2 products can be achieved using g-C_3N_4, a framework with good catalytic activity. Jiao et al. then synthesized Cu-C_3N_4 to provide experimental evidence

for the theoretical calculation of the g-C_3N_4 framework. In the synthesized samples, the analysis from N K-edge NEXAFS spectra and Cu 2p XPS confirmed the great chemical interaction between N and Cu atoms. However, the main product of CO_2RR of Cu-C_3N_4 is still hydrogen (> 50%), which is due to the presence of a huge number of uncoordinated g-C_3N_4 in the heterojunction, resulting in fewer active sites and active hydrogen precipitation reactions on the studied Cu-C_3N_4 materials (Jiao et al., 2017). This suggests that the g-C_3N_4-loaded Cu-based catalysts still need further improvement.

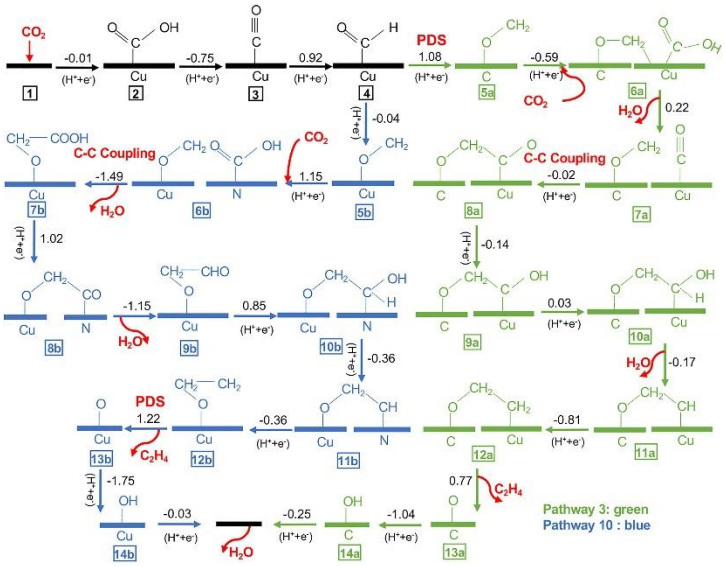

Figure 2.7 Some pathways of electrochemical reduction from CO_2 to C_2H_4 on the catalyst Cu-C_3N_4 (Zhang et al., 2018a).

2.3 Summary

To date, considerable advancements have been made in the field of copper-based catalysts for efficient electrochemical CO_2R for the production of low-carbon fuels and valuable chemicals. Meanwhile, g-C_3N_4-based materials are the most stable phase among all carbon nitride isomers and have also attracted much attention due to their wide application as sustainable multiphase

catalysts for electrocatalysis. This literature review provides an overview of the recent developments of electrochemical CO_2R based with metallic copper and g-C_3N_4, respectively. Mesoporous g-C_3N_4 is able to be utilized as a non-homogeneous catalyst to activate CO_2R systems. However, the study of CO_2R electrocatalysts with g-C_3N_4 as a framework is still in its infancy, and although some theoretical support is available, few experiments have been conducted to systematically verify it. Therefore next, this dissertation innovatively will design a graphite phase carbon nitride loaded copper oxide composites (CuO/g-C_3N_4) based on a simple hydrothermal method, which is important for understanding the explanation of the synergistic mechanism of copper-based catalysts and g-C_3N_4.

CHAPTER III. EXPERIMENTAL

3.1 Materials and Reagents

Urea ($CO(NH_2)_2$), polyvinyl pyrrolidone K30 (PVP-K30), copper(II) nitrate trihydrate ($Cu(NO_3)_2 \cdot 3H_2O$), sodium acetate ($C_2H_3NaO_2$), sodium hydroxide (NaOH), potassium bicarbonate ($KHCO_3$), isopropanol (C_3H_8O), acetone (C_3H_6O), Deuterium oxide (D_2O) and dimethyl sulfoxide (C_2H_6OS) were purchased from Sinopharm Chemical Reagent. Sodium dodecyl sulfate (SDS), ethanol (C_2H_6O, 99.7 %) and spherical cupric oxide particles (CuO, 40 nm, 99.5 %) were purchased from Macklin. Nafion 117 solution (~5%) were purchased from Aladdin. Carbon paper (GDS180S) was purchased from Ce Tech. Carbon dioxide (CO_2, 99.9999 %) was purchased from Linde. Every chemical was used directly as received, and UP water (> 18.2×10^6 Ω·cm) was adopted to dispense the whole aqueous solutions.

3.2 Preparation of Catalysts

3.2.1 Preparation of g-C_3N_4

20 g urea was put into a 50 mL crucible, and after that, the prepared sample was heated for 2 h under air condition in a muffle furnace directly at 550 °C, heating up at a rate of 5 degrees per minute. After letting itself naturally drop to ambient temperature, g-C_3N_4 sample was obtained.

3.2.2 Preparation of CuO nanosheets (CuO NSs)

0.238 g $Cu(NO_3)_2 \cdot 3H_2O$, 0.173 g $C_2H_3NaO_2$, 0.500 g PVP and 0.295 g SDS were dissolved into 100 mL H_2O. Then 0.1 M NaOH were added dropwise

respectively under vigorous stirring until pH >12. The precipitate was obtained by centrifuging the suspension and washed with H_2O many times, and was dispersed into 150 mL solution containing 0.500 g PVP and 0.346 g SDS. The suspension was loaded in a 200 mL Teflon-lined stainless-steel autoclave and heated for 24 hours at 170 °C. The resultant sample was obtained by centrifuging the suspension, repeatedly washing it in H_2O and EtOH, and then heating it to 250 °C (5 °C min^{-1}) and holding it there for two hours in air.

3.2.3 Preparation of CuO/g-C_3N_4

0.500 g PVP and 0.295 g SDS were dissolved into 100 mL H_2O, and 0.100 g g-C_3N_4 was introduced and sonicated for 1.5 h. Then, 9 mL of 0.1 M $Cu(NO_3)_2 \cdot 3H_2O$ and 20 mL 0.1 M $C_2H_3NaO_2$ were added dropwise respectively under continuing stirring. After stirring the suspension for 40 min, 0.1 M NaOH were added dropwise respectively under vigorous stirring until pH>12. The precipitate was gathered by centrifuging the suspension and cleaned repeatedly in H_2O many times, and was dispersed into 150 mL solution containing 0.500 g PVP and 0.346 g SDS. The suspension was placed in a 200 mL Teflon-lined stainless-steel autoclave and heated at 170 °C for 24 hours. The resulting sample was collected by centrifuging the suspension and repeatedly washing it with H_2O and ethanol before being heated to 250 °C, 5 °C min^{-1} and retained for 2 hours.

3.3 Characterizations

The morphology and structure were characterized by field emission scanning electron microscope (FESEM, Regulus 8100, 5 kV) and transmission electron

microscopy (TEM, Tecnai G2 F20, 200 kV). Energy-dispersive X-ray spectroscopy (EDS) mapping were characterized by FESEM Regulus 8100. The chemical state was analyzed by X-ray photoelectron spectroscopy (XPS, Thermo Escalab 250) and the source gun type is Al Kα. X-ray diffraction (XRD) was carried out on D8 Advance produced by German Bruker-AXS. X-ray generator operating at 40 kV and 40 mA at a step of 0.01° (2θ) at room temperature. Fourier Transform Infrared Spectrometer (FTIR) spectra were measured in the 4000-400 cm^{-1} range on Nicolet iS50 FT-IR spectrometer with samples prepared as KBr pellets. Brunauer-Emmett-Teller (BET) surface area measurement was performed at 77 K on TriStar II 3020 adsorption analyzer in N_2-adsorption mode.

3.4 Electrochemical Measurements

3.4.1 Preparation of Working Electrode

The carbon paper was pre-treated with acetone at 25 °C for 15 min, then washed several times with water and EtOH, then air dried. The sample ink was prepared by dispersing 4 mg sample (CuO/g-C_3N_4, CuO NSs or spherical cupric oxide particles (CuO SPs)) and 30 μL Nafion solution into 1 mL isopropanol followed by sonication for 30 min. Then the ink was drop-casted on the pre-treated carbon paper (2 × 2 cm^2) and cut to an area of 1 × 1 cm^2 to use as the working electrode for measurements.

3.4.2 Design of CO_2 Reduction System

In the electrochemical CO_2 reduction reaction, in addition to designing excellent electrocatalysts, the design of the CO_2 reduction electrocatalytic

device is also an effective means to enhance the reaction performance by affecting the current density, product distribution, Faradaic efficiency and catalytic stability.

The H-type electrolytic cell is the most widely used CO_2RR device in the laboratory. Working and reference electrodes are inserted in the cathode chamber and the counter electrode is in the anode chamber, which are connected by prepared electrolyte but divided by an ion exchange membrane to prevent re-oxidation of the reduced products. The working electrode can be either a bulk catalyst or a powder catalyst loaded on carbon paper, CO_2 gas is continuously passed into the cathode chamber during the whole reaction through a gas flow meter and then passed to gas chromatography (GC) for detection of the gas phase products and nuclear magnetic resonance (NMR) for detection of the liquid phase products.

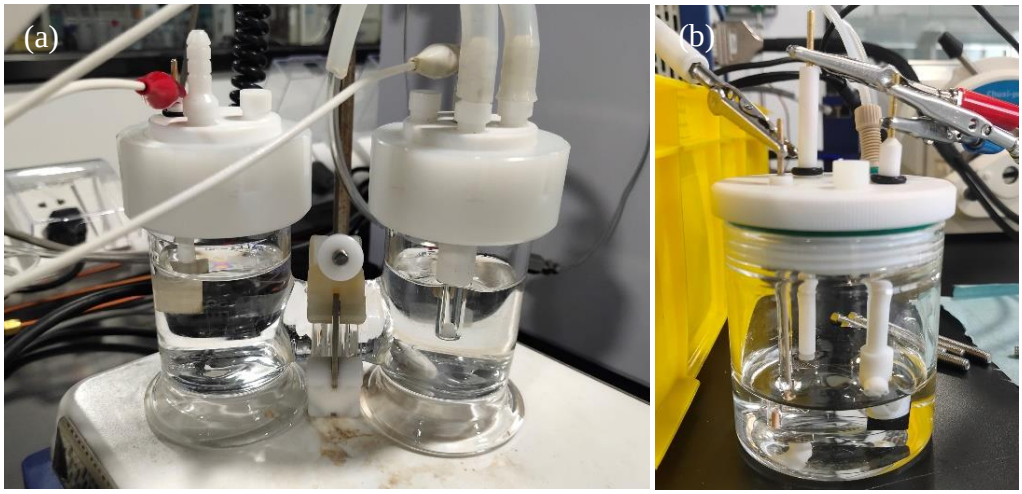

Figure 3.1 (a) H-type electrolytic cell and (b) common sealed electrolytic cell.

3.4.3 Testing Conditions and Calculation Methods

The electrochemical measurements except chronopotentiometry test were performed with a Reference 300 electrochemistry workstation (Gamry) in a three-electrode single-tank setup. Platinum mesh and Ag/AgCl electrode (saturated KCl) were used as reference electrode and counter electrode respectively. CO_2-saturated (pH ≈ 6.8) or Ar-saturated 0.1 M $KHCO_3$ (pH ≈ 8.3) was used as electrolyte. And all potentials measured were calibrated to the reversible hydrogen electrode (RHE) reference scale with manual iR compensation:

$$E_{RHE} = E_{Ag/AgCl} + 0.059 \times pH + 0.205 - iR_u$$

The iR_u was determined by potentiostatic electrochemical impedance spectroscopy measurements under an open circuit potential (OCP) at frequencies ranging from 10^5 Hz to 0.1 Hz. The linear sweep voltammetry (LSV) was tested at a sweep rate of 10 $mV \cdot s^{-1}$, over the potential range from 0.25 to -2.5 V vs. RHE. The current density was calculated by normalizing the current to the corresponding geometric surface area. Electrochemical impedance spectroscopy (EIS) measurement was carried out in the frequency range of 10^5 to 0.01 Hz at OCP and the magnitude of the modulation signal was 5 mV. The measured EIS data were then fitted by a simplified Randles equivalent circuit using Gamry Echem Analyst software. ECSA was determined by the double-layer capacitance method. The potential range was 0.05 to 0.06 V vs. RHE, and cyclic voltammetry curves were performed at different sweep speeds.

The chronopotentiometry test (CP) were performed with a Reference 300 electrochemistry workstation in a H-type electrolytic cell (C007, Gaoss Union), which consists of two compartments separated by Nafion 115 membrane. Platinum and Ag/AgCl electrode (3.5 M KCl) were used as counter electrode and reference electrode respectively. CO_2-saturated 0.1 M $KHCO_3$ (pH ≈ 6.8) was used as electrolyte. The constant potential electrolysis was performed by measuring the I-t curve with the horizontal and vertical coordinates of time (s) and current density ($mA \cdot cm^{-2}$) respectively, imposing different applied voltages and setting the test time to 7200 s. During the electrolysis, CO_2 gas was always introduced into the cathode electrolyte at a rate of 30 $mL \cdot min^{-1}$, and the CO_2 gas flow rate was controlled by a gas flow meter. During the test, the sample was fed every 7 min on average, and the last sample was selected as the final result. The resulting gas phase products were detected by gas chromatography (Agilent GC 8890) with high purity N_2 as the carrier gas, mainly by two detectors: thermal conductivity detector (TCD) and hydrogen flame ionization detector (FID), where TCD is commonly used for the detection of H_2 components and FID is mainly used for the detection of hydrocarbons in the products. CO gas cannot be directly detected by FID and needs to be converted to methane by a methane reformer before detection. The electrochemical CO_2 reduction products are not only a gas-phase mixture, but also a liquid phase products containing carbon, which is detected by NMR (AVANCE III HD 400 MHz). 500 μL of electrolyte is pipetted into the NMR tube, and DMSO is used as an internal standard. Deuteroxide is also added and disperse them well. This internal standard was added to the NMR tube containing the electrolyte for nuclear magnetic hydrogen spectroscopy (^1H

NMR) testing. According to the results of the NMR spectra, different peak positions corresponded to different groups, and then the concentration of each liquid phase product was determined by the ratio of the peak area of DMSO to the peak area of the product.

The Faradaic efficiency of gas products was performed using following equation:

$$FE_{gas} = \frac{nCGP \times 96485}{ITR}$$

n is the quantity of e^- transferred to product formation. *C* is the concentration (ppm) of the gases revealed by GC. *G* is flow rate of CO_2. *I* is the cell current. *P* = 1.01×10^5 Pa. *T* = 273.15 K. *R* = 8.314 J·mol·K^{-1}.

The Faradaic efficiency of liquid products is calculated by following equation:

$$FE_{liquid} = \frac{cV \cdot ne \times 6.022 \times 10^{23}}{\frac{Q}{e}}$$

c is the concentration of product. *V* is the total volume of cathodic electrolyte. *n* is the quantity of e^- transferred to product formation. *e* is electron. *Q* is the number of transfer charge.

Partial current density is calculated based on the following equation:

$$j = j_{total} \times FE$$

j_{total} is the cell current. *FE* is the Faradaic efficiency of each product.

CHAPTER IV. RESULTS and DISCUSSION

PART I - MORPHOLOGY and STRUCTURE CHARACTERIZATIONS

The morphology and structure of CuO NSs, g-C_3N_4, and CuO/g-C_3N_4 composites were confirmed using FESEM. It can be seen that a large number of CuO nanosheets of varying lengths were synthesized in Figure 4.1 (a), with an average width of about 300 nm. In Figure 4.1 (b), pure g-C_3N_4 is composed of irregular and loose aggregates of sheet-like structures. The lamellae formed as a result of the thermal breakdown of urea fracture while producing a large number of pores, and this rough appearance confers a very high functionalization on the g-C_3N_4 sheets. Figure 4.1 (c) demonstrates that when it comes to the CuO/g-C_3N_4 composites, it is evident that the particles with smooth surfaces in connected sheets of agglomerates are considered as CuO NSs loaded on the g-C_3N_4 matrix. The particles were deposited uniformly on the carbon fibers, although some agglomeration of particles was observed (Figure 4.1 (d)). In Figure 4.1 (e), the particles on carbon paper shows no obvious morphological changes compared to before coating, and only the size decreased, indicating that the ultrasonic dispersion process did not destroy the structure of the catalysts and CuO/g-C_3N_4 has a strong stability. However, the electrochemical reduction leads to further dispersion and regular dense arrangement of the particles (Figure 4.1 (f)). The newly created nanoparticles have a particle size of only about 100 nm, and the exposure of more active centers facilitates the coupling of C-C bonds. A similar phenomenon is observed on CuO NSs loaded carbon paper (Figure S1). The corresponding

EDS spectra (Figure 4.2 (f)) indicate that the composites are consist of C, N, O, and Cu elements. Meanwhile, the corresponding elemental mapping (Figure 4.2 (b)-(e)) also shows that the O, N, C, and Cu atoms are evenly distributed throughout the composite, indicating the emergence of the CuO/g-C_3N_4 structure and the close-contact between them.

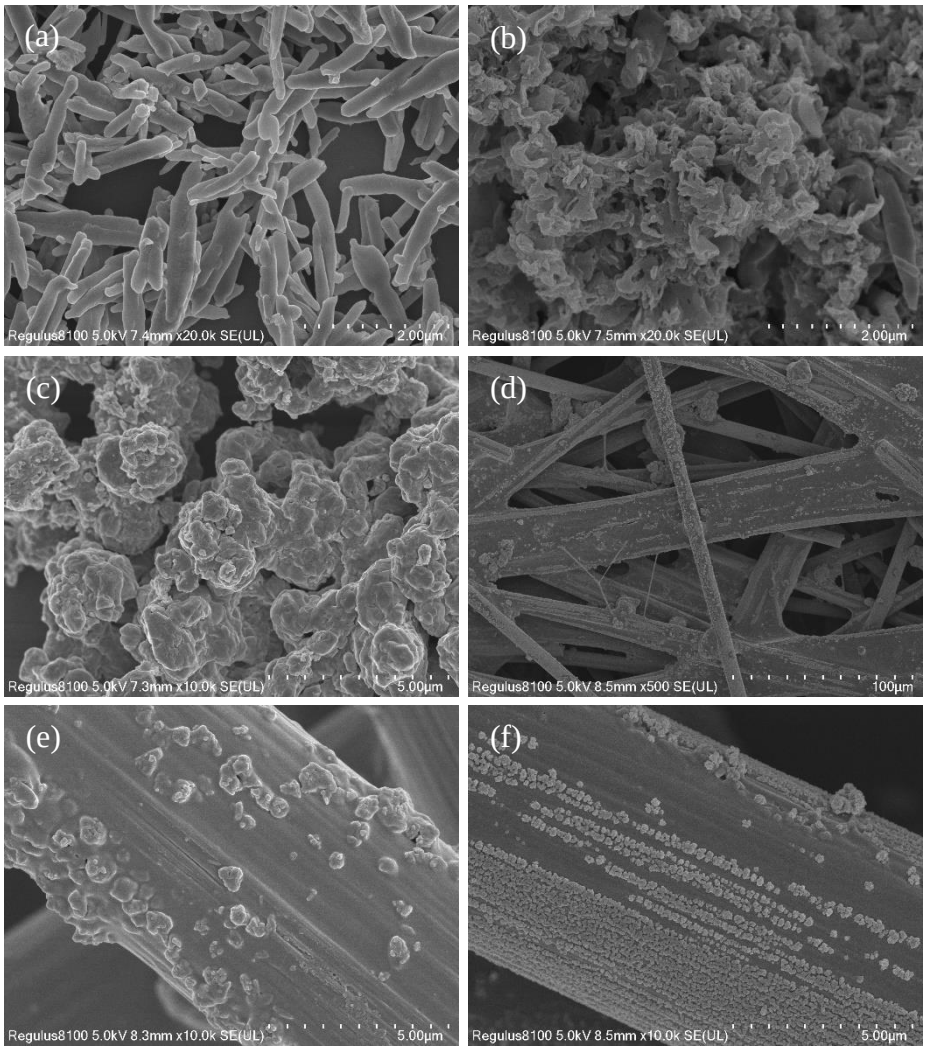

Figure 4.1 FESEM images of (a) CuO NSs, (b) pure g-C_3N_4, (c) CuO/g-C_3N_4, CuO/g-C_3N_4 loaded on carbon paper (d and e) before reduction and (f) after 2 h reduction.

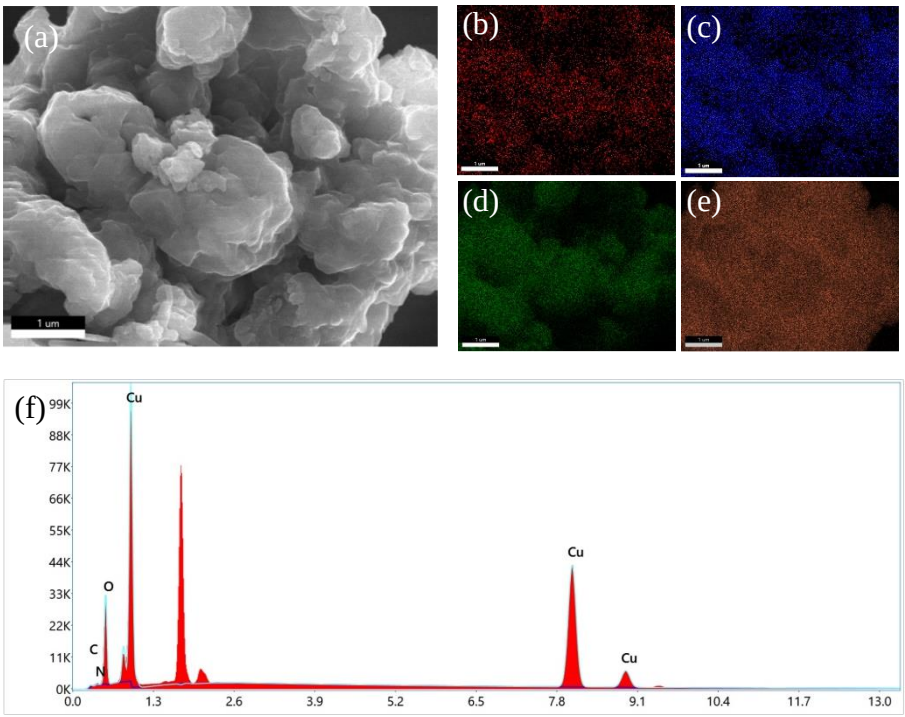

Figure 4.2 (a) SEM image, and elemental mapping of (b) C, (c) N, (d) O (e) Cu, and (f) EDS spectroscopy of CuO/g-C_3N_4.

TEM has been used to more clearly view the microstructure and morphology of simple g-C_3N_4 sheets, CuO NSs, and CuO/g-C_3N_4 hybrids. We can see that the g-C_3N_4 sheet shows a folded two dimensional sheet with a single or several layers (Figure 4.3 (a)). This particular structure leads to a great surface area, acting as a support to bind other particles. The TEM images of CuO NSs (Figure 4.3 (b)) show clear long lamellar shapes and CuO SPs (Figure 4.3 (c)) show nanoparticles about 40 nm respectively. Meanwhile, Figure 4.3 (d) depicts a clear outline of g-C_3N_4 with CuO coating its surface. The HRTEM image of CuO in Figure 4.3 (e) shows the presence of two different interplanar distances, 0.231 and 0.255 nm, referring to the two standard CuO planes: (200) and (002) respectively. Likewise, the selected area electron diffraction (SAED)

pattern of CuO/g-C_3N_4 was obtained, as shown in Figure 4.3 (f). The diffraction rings from center to edge separately denote CuO (001), CuO (002), CuO (200), CuO (111) and CuO (-202), illustrating a highly crystallized CuO structure. These results demonstrate that the CuO sample in the prepared composite is composed of polycrystals.

The crystal phase of the synthesized catalysts was revealed by the XRD patterns. According to Figure 4.4, the (100) and (002) diffraction planes of the graphitic materials correspond to the two typical diffraction peaks of pure g-C_3N_4 at 13.08° and 27.17°, which are brought on by the in-plane structure of the tri-s-triazine motifs and the interlayer stacking of conjugated aromatic rings (Mao et al., 2017). In terms of CuO NSs, the main peaks at 32.50°, 35.50°, 38.73°, 38.96° and 48.73° can be indexed to the crystal facets (-110), (002), (111), (200) and (-202) of CuO (JCPDS # 45-0937). CuO/g-C_3N_4 composite allows for the observation of both the g-C_3N_4 and CuO diffraction peaks, proving that the two elements coexist in the material. The lack of any additional distinctive peaks reveals the high purity of the samples right after preparation.

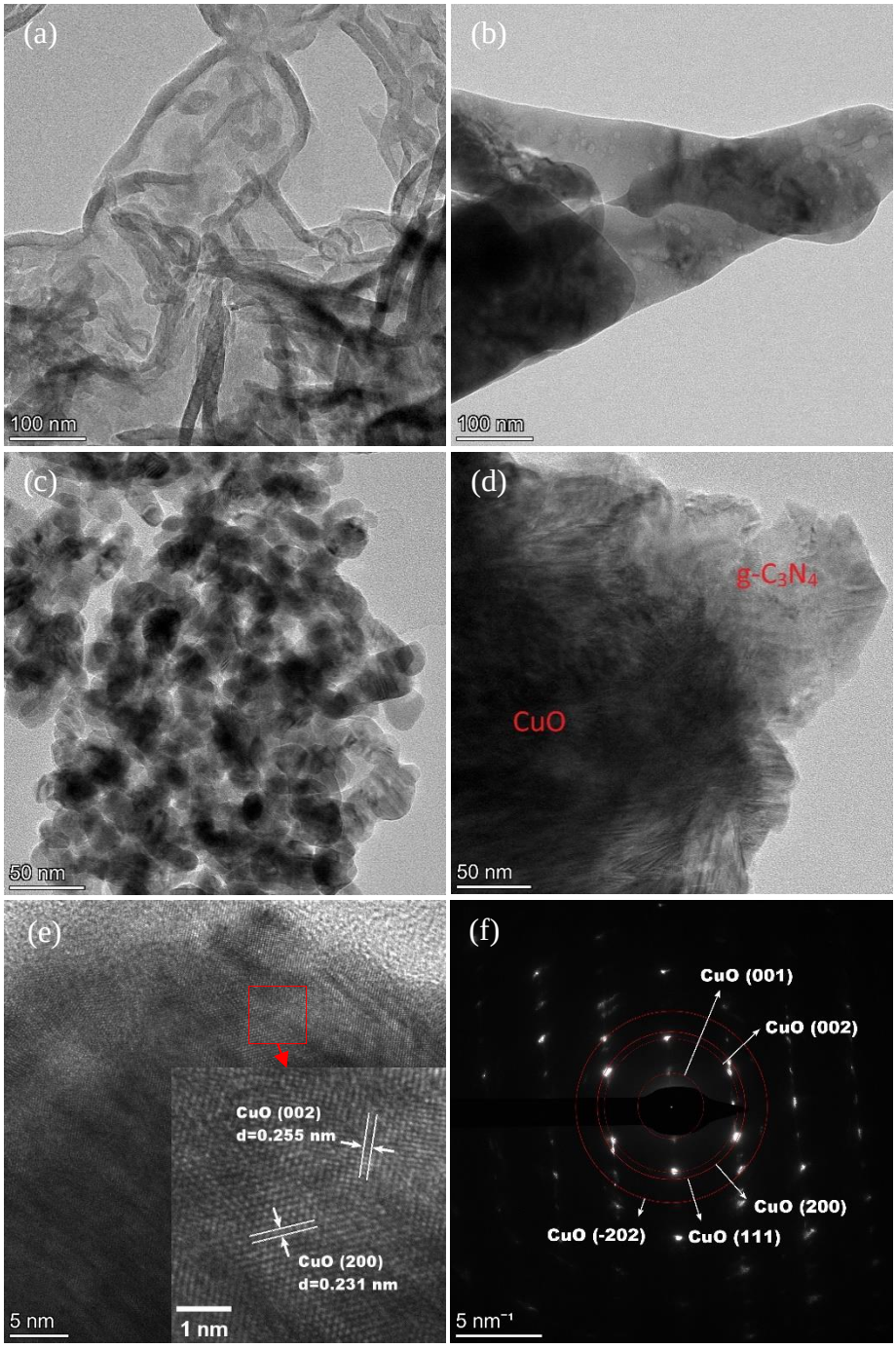

Figure 4.3 TEM images of (a) g-C_3N_4, (b) CuO NSs, (c) CuO SPs, (d) CuO/g-C_3N_4 and HRTEM and SAED patterns of CuO/g-C_3N_4 (e and f).

To further assess the phase formation of each component and to ascertain the existence of the functional groups bonded to the layer of the catalysts, the FTIR

spectra of three catalysts: CuO/g-C_3N_4, g-C_3N_4 and CuO NSs are shown in Figure 4.5. The broad band at about 3180 cm^{-1} for g-C_3N_4 is caused by N-H stretches. The cluster bands between 1248 and 1631 cm^{-1} can be classified as the classic stretching mode of C-N heterocycles, in terms of g-C_3N_4, fully condensed bridging units C-NH-C or trigonal units C-N(-C)-C. The heptazine ring system is the source of the 805 cm^{-1} sharp peak. The distinctive bands seen in CuO NSs at 425 cm^{-1} correspond to the CuO Au mode, and at a slightly higher wavenumber position, i.e. 496 cm^{-1} and 605 cm^{-1}, is Bu mode and other Bu mode, respectively. The peak of Cu-O stretching vibration is also very obvious, vibration along the [101] direction, is at 496 cm^{-1}. Another high-frequency mode at 605 cm^{-1} may be attributed to the perpendicular [101] direction. The absorption peak at 1630 cm^{-1} comforms to HOH bending mode and peak at 3435 cm^{-1} comforms to O-H stretching vibration. Both of them reflect adsorbed water molecules, since the nanocrystalline materials possess considerable specific surface area, leading to the absorption of moisture in the lattice. The common peaks in the spectra of g-C_3N_4 and CuO/g-C_3N_4 as well as that of CuO NSs and CuO/g-C_3N_4 are due to the contribution from the g-C_3N_4 and CuO phase (Bhattacharjee and Ahmaruzzaman, 2015, Li et al., 2010, Kliche and Popovic, 1990, Zheng and Liu, 2007).

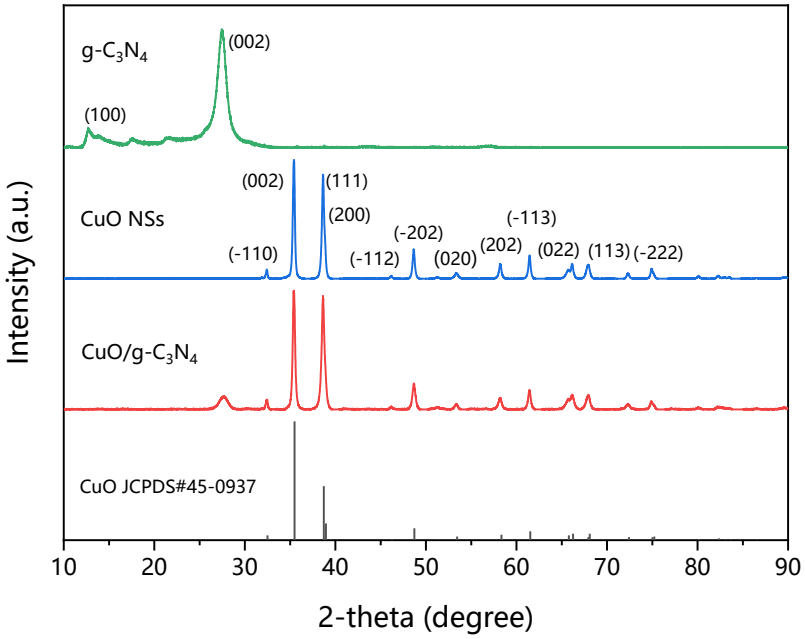

Figure 4.4 XRD patterns for g-C_3N_4, CuO NSs and CuO/g-C_3N_4.

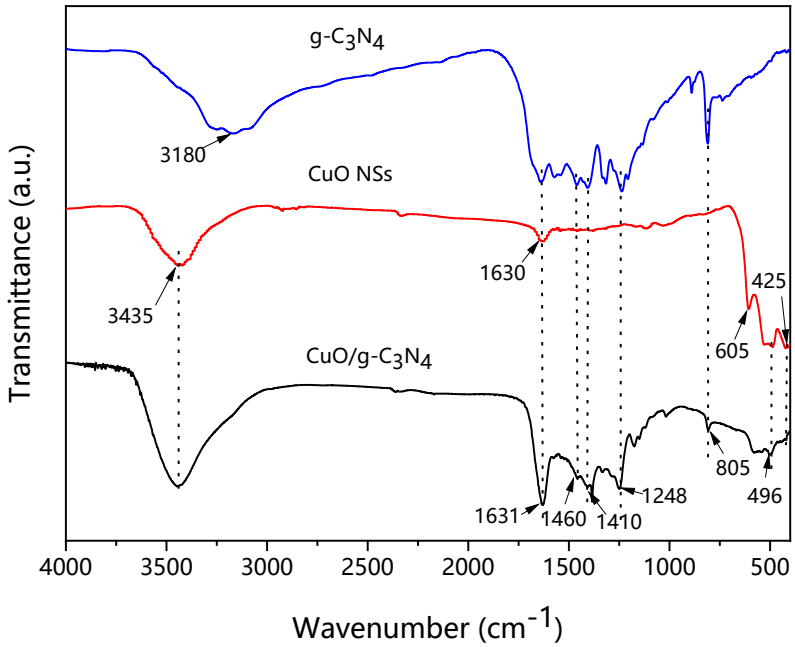

Figure 4.5 FTIR spectra of g-C_3N_4, CuO NSs and CuO/g-C_3N_4.

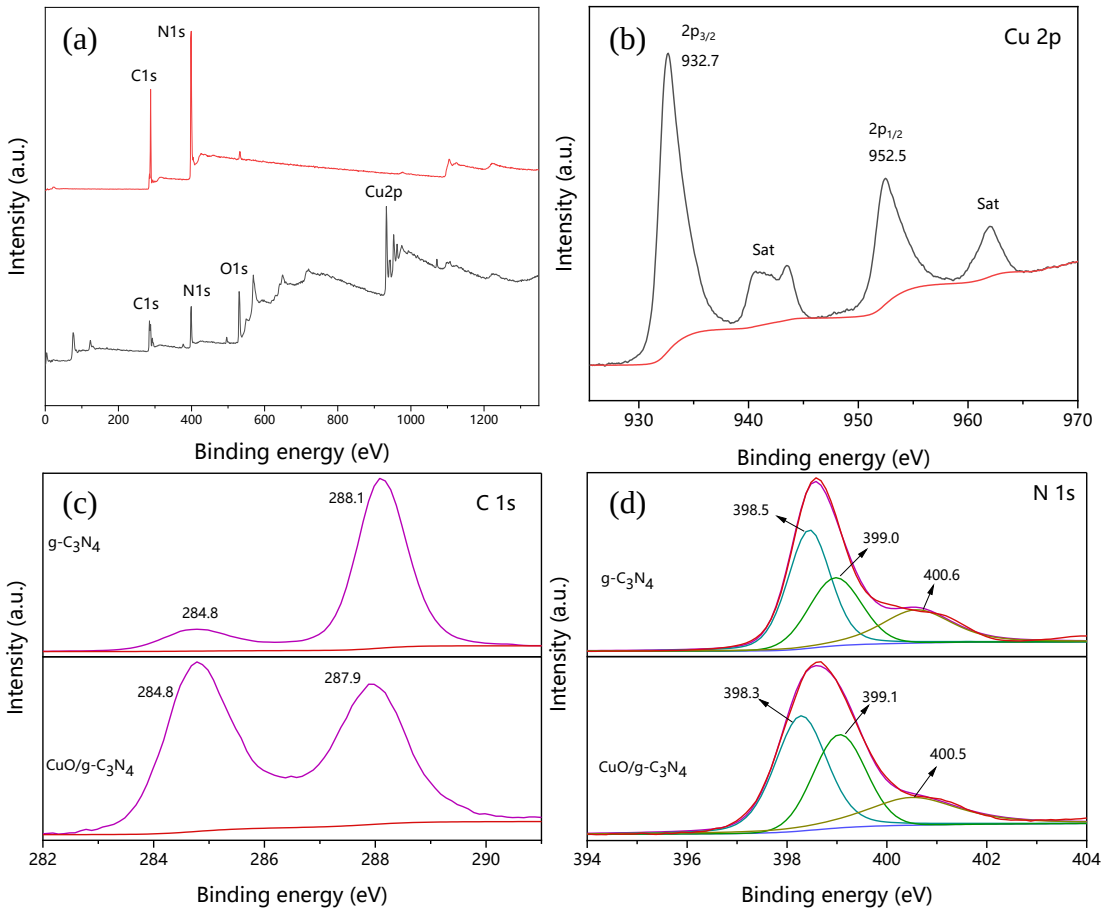

Figure 4.6 XPS spectra of g-C_3N_4 and CuO/g-C_3N_4: (a) full scan, (b) Cu 2p, (c) C 1s, (d) N 1s.

The elemental compositions of g-C_3N_4 and CuO/g-C_3N_4 were examined by XPS spectroscopy and the binding energies obtained for each of them were compared. The investigated spectra in Figure 4.6 (a) confirm all anticipated elements are present, namely N 1s, C 1s for g-C_3N_4 and O 1s, Cu 2p, N 1s, and C 1s for CuO/g-C_3N_4. In Figure 4.6 (b), Cu 2p high-resolution peak of composite CuO/g-C_3N_4 was studied. The pattern of CuO/g-C_3N_4 with a couple of peaks discovered at 932.7 and 952.5 eV that are associated with two typical energy levels of copper: $2p_{3/2}$ and $2p_{1/2}$. CuO crystals are present according to the nearly 20 eV spin-orbit energy difference. This also indicates that the Cu in

the sample is in the +II oxidation state. The small peaks at about 940 ~ 945 eV are satellite peaks, which are generally seen in Cu ions in the oxidation state of +II. Furthermore, in Figure 4.6 (c), a C 1s binding energy peak is assigned at 284.8 eV for both g-C_3N_4 and CuO/g-C_3N_4, belonging to the C=N sp^2 bond and the interaction of the metal oxide with g-C_3N_4 in the composite. Similarly, on the s-triazine ring of graphitic nitride for g-C_3N_4 and CuO/g-C_3N_4, there are sp^2 N-C=N bonds, which can be represented by the C 1s peaks at 288.1 and 287.9 eV. Assigned to the graphitic N, pyrrolic N, and pyridine N, respectively, the g-C_3N_4 N 1s peak can be deconvoluted into three fitted peaks at 400.6, 399.0 and 398.5 eV. Pyridine N binding energy in the CuO/g-C_3N_4 sample (398.3 eV) is 0.2 eV lower than it is in pure g-C_3N_4 (398.5 eV), impacting the interaction between the two molecules at the interface (Figure 4.6 (d)). According to DFT calculations, this effect reduces the free energy of the initial hydrogenation step of CO_2 reduction, i.e. CO_2 to *COOH, which can be attributed to the enhanced adsorption of *CO by g-C_3N_4. In the *CO adsorption step, the distance of the element N which is an adsorption center, and C on the intermediate *CO, is much smaller than that of the other nitrogen-doped carbon materials, and this can also be seen from the calculation that the bond length of the CO triple bond (112.8 pm) is stretched to converge to the double bond length (115.6 ppm). This leads to a significant decrease in the free energy of the reaction in this step. The subsequent reactions give rise to intermediates such as *OCH_2, *CH_2OH, etc., which in turn produce a variety of C_2 products. This process shows the migration of the original Cu-intermediate C active center from Cu to C in g-C_3N_4, depending on the reaction free energy at different sites. This two-center mechanism induces the transfer of CO_2 to multi-carbon compounds

(Duan, 2018, Zhao et al., 2019, Li et al., 2019, Fu et al., 2018b, Cao et al., 2014, Sun et al., 2015).

The surface characteristics of the nano-adsorbent can be identified using BET, which is regarded as an important analysis. It is directly related to the adsorbent's adsorption capacity. The obtained isotherm has been classified as a type III isotherm with mesoporous characteristics by the International Union of Pure and Applied Chemistry (IUPAC). (Figure 4.7 (a) and (b)). BET surface area of g-C_3N_4 and CuO SPs as obtained are 87.6 m^2/g and 37.7 m^2/g, and CuO NSs is 7.62 m^2/g. Meanwhile, BET surface area of CuO/g-C_3N_4 as obtained is 11.2 m^2/g. It is inferred that because CuO nanosheets are attached to the pores of g-C_3N_4, the specific surface area CuO/g-C_3N_4 samples are reduced compared with pure g-C_3N_4. Compared to CuO SPs, the specific surface area of CuO/g-C_3N_4 is smaller and it can be assumed that the specific surface area is not a determinant of catalytic performance.

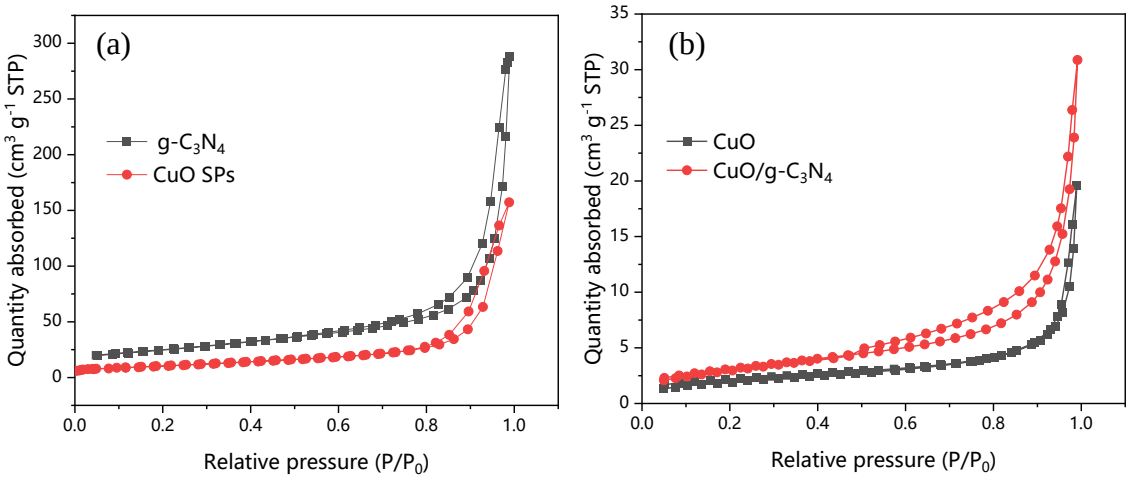

Figure 4.7 N_2 adsorption-desorption isotherms of (a) g-C_3N_4 and CuO SPs, (b) CuO NSs and CuO/g-C_3N_4.

CHAPTER V. RESULTS and DISCUSSION

PART II - ELECTROCHEMICAL MEASUREMENTS

5.1 Electrochemical Activity Tests

LSV curves of CuO SPs, CuO NSs and CuO/g-C_3N_4 catalysts in Ar- and CO_2-saturated 0.1 M $KHCO_3$ solutions are displayed (Figure 5.1). In the CO_2-saturated electrolyte, obviously, all of the investigated catalysts show higher current densities compared to those in the Ar-saturated electrolyte, demonstrating their great inherent activity for electrochemical CO_2R. Under the same solution condition, CuO/g-C_3N_4 also exhibited a smaller onset potential than CuO NSs and CuO SPs. And CuO/g-C_3N_4 also exhibits a noticeably improved current density from onset potential to -2.5 V vs. RHE, relative to the other two catalysts, thus implying its higher CO_2RR performance.

To provide understanding into the CO_2R mechanism on the CuO/g-C_3N_4 catalysts surface, Tafel curves for the overpotential-log (C_2 current density) were plotted. Figure 5.2 was gained by fitting the Tafel equation, the overpotential η is equal to m × log (i) + n, where i is the applied current density and m is what we focus on: Tafel slope. Tafel slope, which symbolizes the section of the strong polarization region in the polarization curve, can be used to further examine the CuO/g-C_3N_4 catalyst's intrinsic activity in the electrochemical CO_2R process. The slopes show that the rate of CO_2R

increases more rapidly with growing potential. Then, the slopes of the curves for CuO/g-C_3N_4, CuO NSs and CuO SPs were 17.2 mV·dec^{-1}, 27.8 mV·dec^{-1} and 33.6 mV·dec^{-1}. Compared with CuO NSs and CuO SPs, the slopes of CuO/g-C_3N_4 exhibit a significant decrease, which is further evidence of the better intrinsic properties of the CuO/g-C_3N_4 surface. However, the Tafel slope of the catalysts CuO/g-C_3N_4 rises rapidly to 98.3 mV dec^{-1} over a larger overpotential range, which shows a qualitative change in the electrochemical CO_2RR process after the overpotential achieves 0.35 V. The slope values above indicate a change in the CO_2 electroreduction's limiting elements. First, as the voltage applied to the electrode increases, the segment of the CuO catalyst is turned easily to Cu_2O and Cu after gaining electrons. This change causes the catalyst structure, like kinks, sidewalls, nanocrystal clusters and angles, which are favorable for the reaction, to disappear, reducing its catalytic performance. In addition, the rate at which reactants and products of reactions are mass transferred within the macroporous structure of catalysts during the electroreduction reaction becomes a significant reaction-limiting factor as overpotential rises, which leads to a sharp increase in the Tafel slopes (Hu et al., 2021).

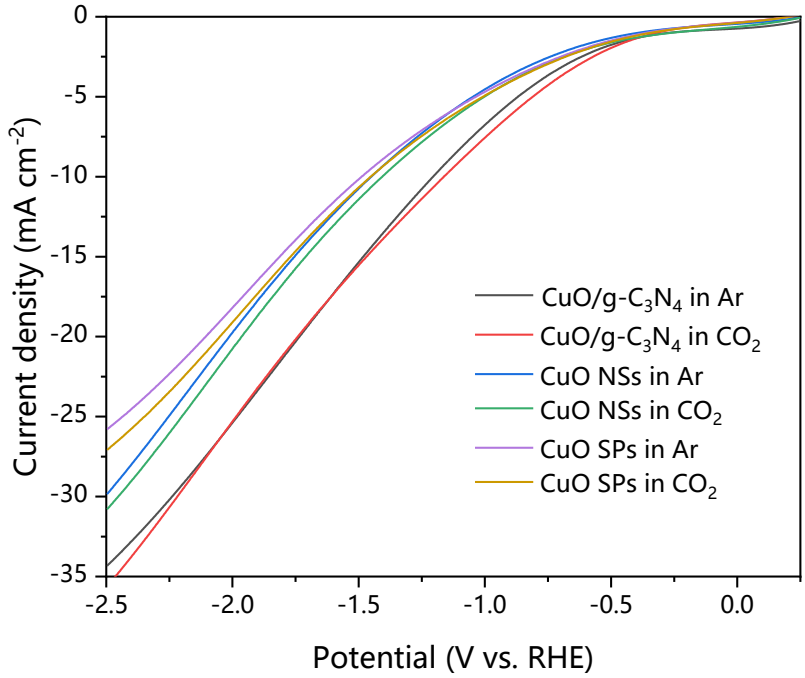

Figure 5.1 LSV curves of CuO SPs, CuO NSs and CuO/g-C_3N_4 catalysts with a scan rate of 10 mV·s^{-1} in Ar- and CO_2-saturated 0.1 M $KHCO_3$ solution.

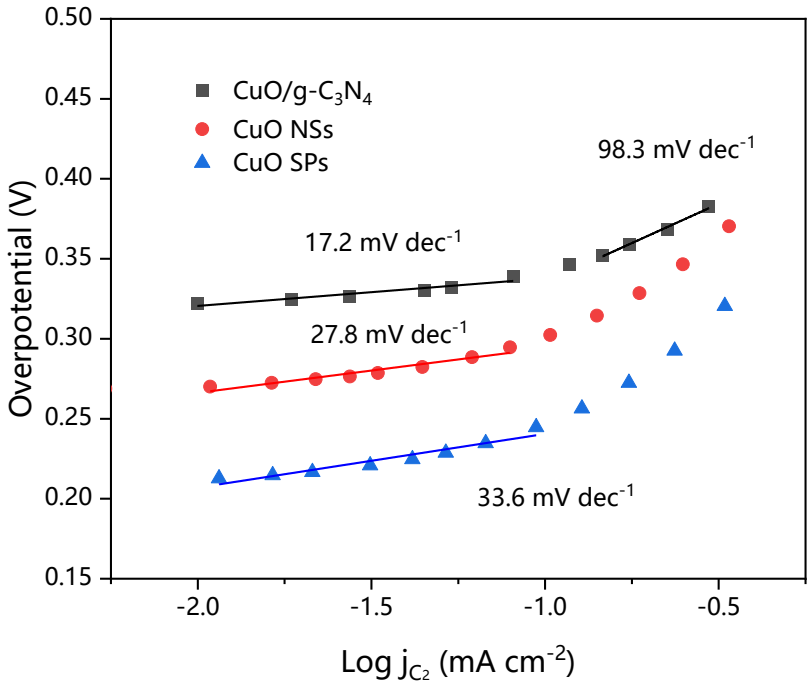

Figure 5.2 Tafel slope calculation curves of CuO SPs, CuO NSs and CuO/g-C_3N_4 in CO_2-saturated $KHCO_3$ solution.

EIS measurements were also performed in CO_2-saturated $KHCO_3$ solution to further investigate the effect of conductivity on electrochemical CO_2R. The results obtained are illustrated using Nyquist plots. According to Figure 5.3, the low value of the x-axis, i.e. before the semicircle, indicates the solution resistance (R_s), and the radius of the fitted arc represents the charge transfer resistance (R_{ct}). At the open circuit potential, the semicircle of the CuO/g-C_3N_4 electrode is smaller than that of the CuO NSs electrode, and both are significantly smaller than the CuO SPs. An equivalent circuit was fitted using the Randles circuit, which consists of the active solution resistance with the constant phase angle element (CPE) and R_{ct} plus the Warburg element (W) in parallel combination in series (Figure S4). The fitting results (Table S2) clearly show that the CuO NSs electrode (702.5 Ω) has a higher charge transfer resistance than the CuO/g-C_3N_4 electrode (361.8 Ω) and a lower charge transfer resistance than the CuO SPs (1722 Ω). The EIS results confirm the high conductivity of the CuO nanosheets, while g-C_3N_4 further enhances the electrocatalytic activity for CO_2 reduction, reflecting the improved charge transfer process at the interface of electrode and electrolyte in the CuO/g-C_3N_4 system.

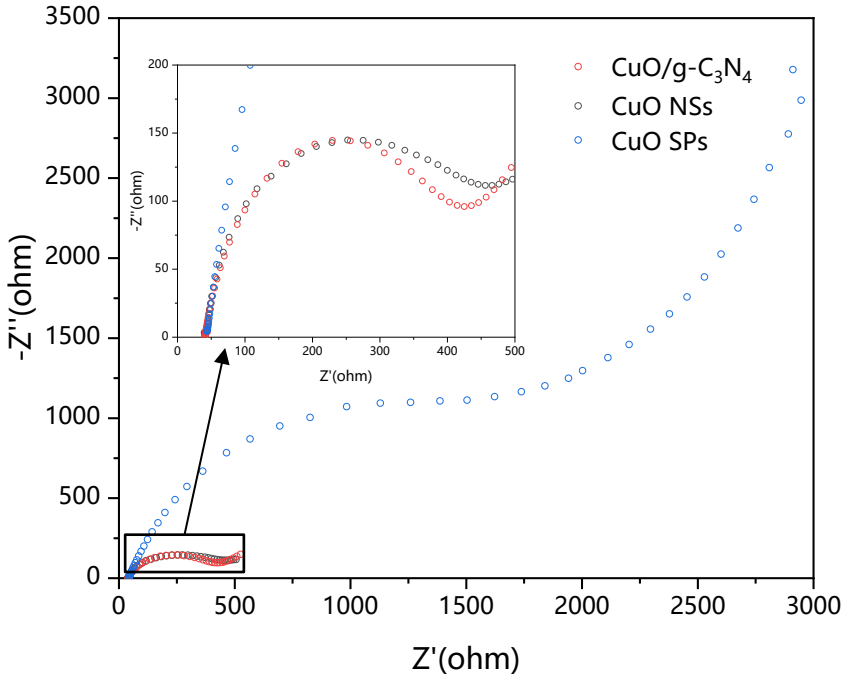

Figure 5.3 EIS spectra of CuO SPs, CuO NSs and CuO/g-C_3N_4 in CO_2-saturated $KHCO_3$ solution. The enlarged Nyquist plots for the high frequency region are displayed in the inset.

The ECSA of CuO SPs, CuO NSs and CuO/g-C_3N_4 electrodes were studied by contrasting the corresponding C_{dl} (double-layer capacitance). CVs of these three electrodes were run in a potential range of 50~60 mV vs. RHE at various scan rates (starting from 20 to 120 $mV \cdot s^{-1}$) (Figure S5), and the slope of non-faradaic capacitive current (current density at 55 mV) versus scan rate was used to calculate the C_{dl} value. According to the formula ECSA = C_{dl}/C_s, ECSA is proportional to C_{dl}, so bigger C_{dl} means larger ECSA. In Figure 5.4 and Table S3, we can see that the C_{dl} of CuO/g-C_3N_4 (55.7 $\mu F \cdot cm^{-2}$) is much higher than that of CuO NSs (39.3 $\mu F \cdot cm^{-2}$), indicating that CuO/g-C_3N_4 has more exposed active sites and a larger electrochemical active surface area, which is advantageous for boosting the CO_2 reduction activity. This also

proves that the larger active surface area is caused by the g-C_3N_4 carrier. Meanwhile, the C_{dl} of CuO NSs are larger than those of CuO SPs (23.1 $\mu F \cdot cm^{-2}$), suggesting that the nanosheets of CuO provide a larger active surface area than commercial spherical nanoparticles of CuO.

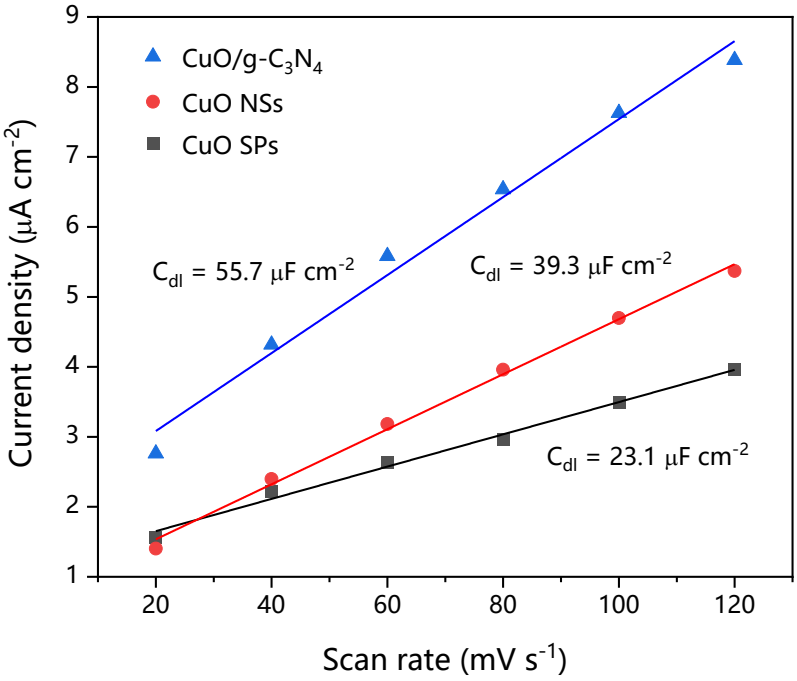

Figure 5.4 Capacitive current at OCP as a function of scan rate for CuO SPs, CuO NSs and CuO/g-C3N4 electrodes.

5.2 Electrochemical CO_2 Reduction Performance Tests

Further, the CO_2RR gaseous products distribution of CuO SPs, CuO NSs and CuO/g-C_3N_4 were comparatively studied at a potential region of -0.8 ~ -1.2 V vs. RHE (Figure 5.5). As shown in Figure 5.5 (a), CuO SPs consistently prefer CH_4 production in all testing potential regions (-0.8 to -1.2 V vs. RHE), while C_2H_4 selectivity is really low (< 20%). This result indicates that regardless of the applied potentials, the C-C coupling activity of CuO SPs is not very high.

Comparatively to CuO SPs, where it is not higher than 5% at any applied potentials, the Faradaic efficiency of CH_4 is suppressed for CuO NSs. At the best potential of -1.0 V vs. RHE, the C_2H_4 production increase from 16.5 % to 31.7 %, and some ethane is formed as well (Figure 5.5 (b)). However, for CuO/g-C_3N_4 electrocatalysts, the CH_4 and CO productions are further considerably suppressed, totaling less than 6 % at -1.0 V vs. RHE, as Figure 5.5 (c) shows. Meanwhile, the CuO NSs catalyst has an 8.1 % Faradaic efficiency of C_1 gaseous products at the same potential. In the meantime, the C_2H_4 selectivity in CuO/g-C_3N_4 is significantly improved, whereas the H_2 production from the HER side reaction is clearly weakened. Particularly at -1.0 V vs. RHE, the C_2H_4 Faradaic efficiency reach as high as 37.0 %, which is accompanied with Faradaic efficiency for H_2 formation as 25.8 %. A very small amount of HCOOH (8.8 %) is also detected at -1.0 V vs. RHE in the liquid product. Ethanol was reliably detected at -0.8 ~ -1.2 V vs. RHE. At -0.8 ~ -1.0V vs. RHE, its Faradaic efficiency varies in a small range of 27.3 ~ 28.2 %. The Faradaic efficiency for C_2 products is 64.7 % for CuO/g-C_3N_4 under the respective optimal potential for C_2 electroproduction. Compared to CuO SPs, CuO NSs and other catalysts in the literature (Table 5.1), CuO/g-C_3N_4 catalysts achieve a further improvement in C_2 selectivity, suggesting that g-C_3N_4 carrier drives the electrochemical reduction of CO_2 to C_2 products.

Partial current density for C_2 formation is a crucial factor when assessing the performance of an electrode for the CO_2RR to C_2 products, because it considers both electrode activity and selectivity. Figure 5.6 (a) compares the

geometric partial current densities for H_2 formation at various electrodes. Overall, negative potential shifts cause the electrode to reach a higher H_2 partial current density. At each potential, the H_2 formation rate at the electrodes follows the trend: CuO/g-C_3N_4 < Cu NSs < CuO SPs, illustrating H_2 production from the competing HER was well controlled on CuO/g-C_3N_4 electrode. However, the partial current density of C_2H_4 shows very different results in Figure 5.6 (b). The curve increased from -0.8 to -1.0 V vs. RHE, followed by the decrease of current density from -1.0 to -1.2 V vs. RHE in general. The maximum C_2H_4 partial current density occurred in CuO/g-C_3N_4, reaching 14.0 $mA \cdot cm^{-2}$. A similar trend could be seen in Figure 5.6 (c): -1.0 V vs. RHE for the best C_2 partial current density (24.5 mA cm^{-2}).

CuO/g-C_3N_4 has excellent activity and selectivity in addition to having decent stability. Its chronoamperometric response is shown in Figure 5.7 when polarized for two hours at -1.0 V (corresponding to its maximum C_2H_4 selectivity). The total cathodic current density trend is really stable, and even remains at 37.0 $mA \cdot cm^{-2}$ at the terminal of the stability test. Its corresponding C_2H_4 selectivity experiences an initial increase then retains over 37.0 % throughout the test.

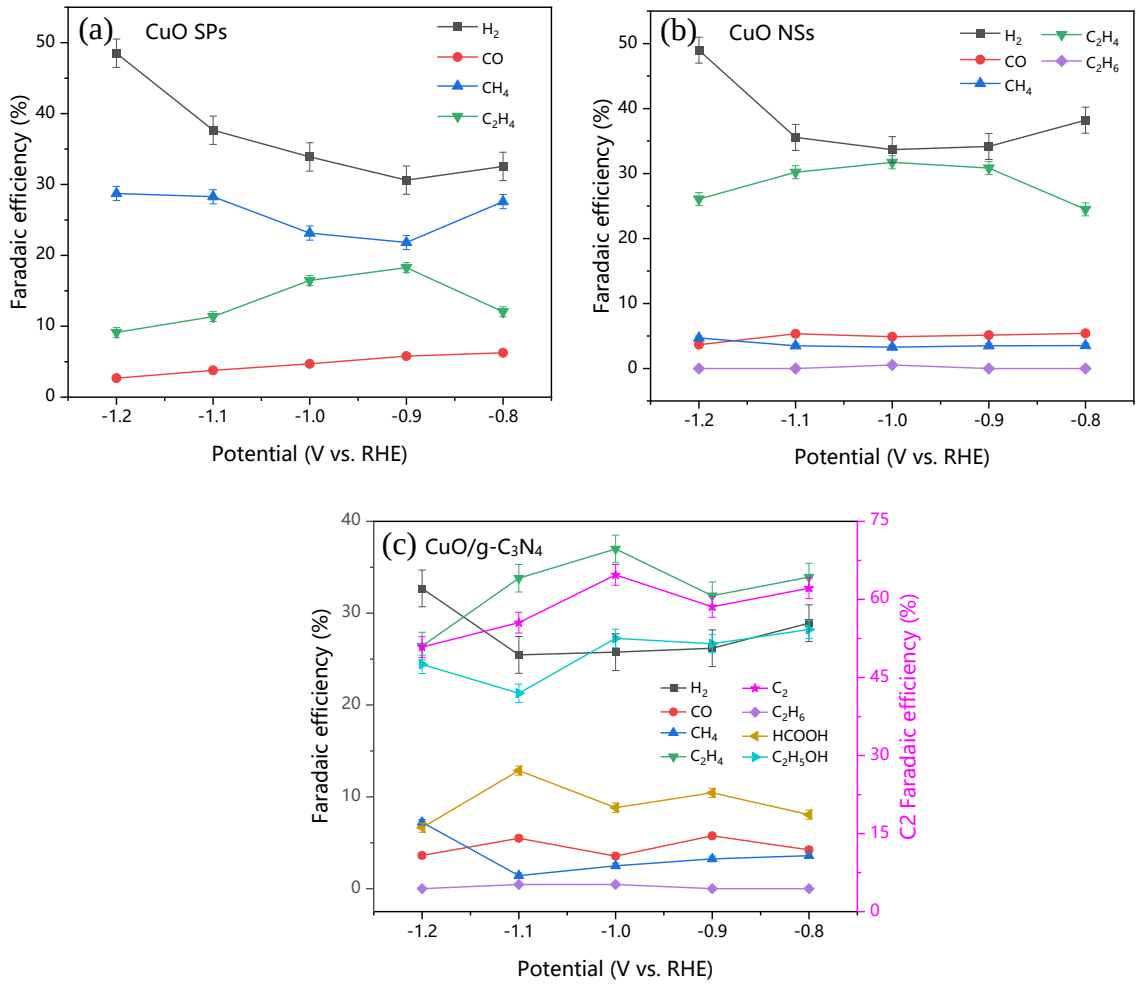

Figure 5.5 Faradaic efficiency of CO_2 electroreduction products as a function of potential. (a) CuO NSs, (b) CuO SPs and (c) CuO/g-C_3N_4. Electrolyte: CO_2-saturated 0.1 M $KHCO_3$ solution.

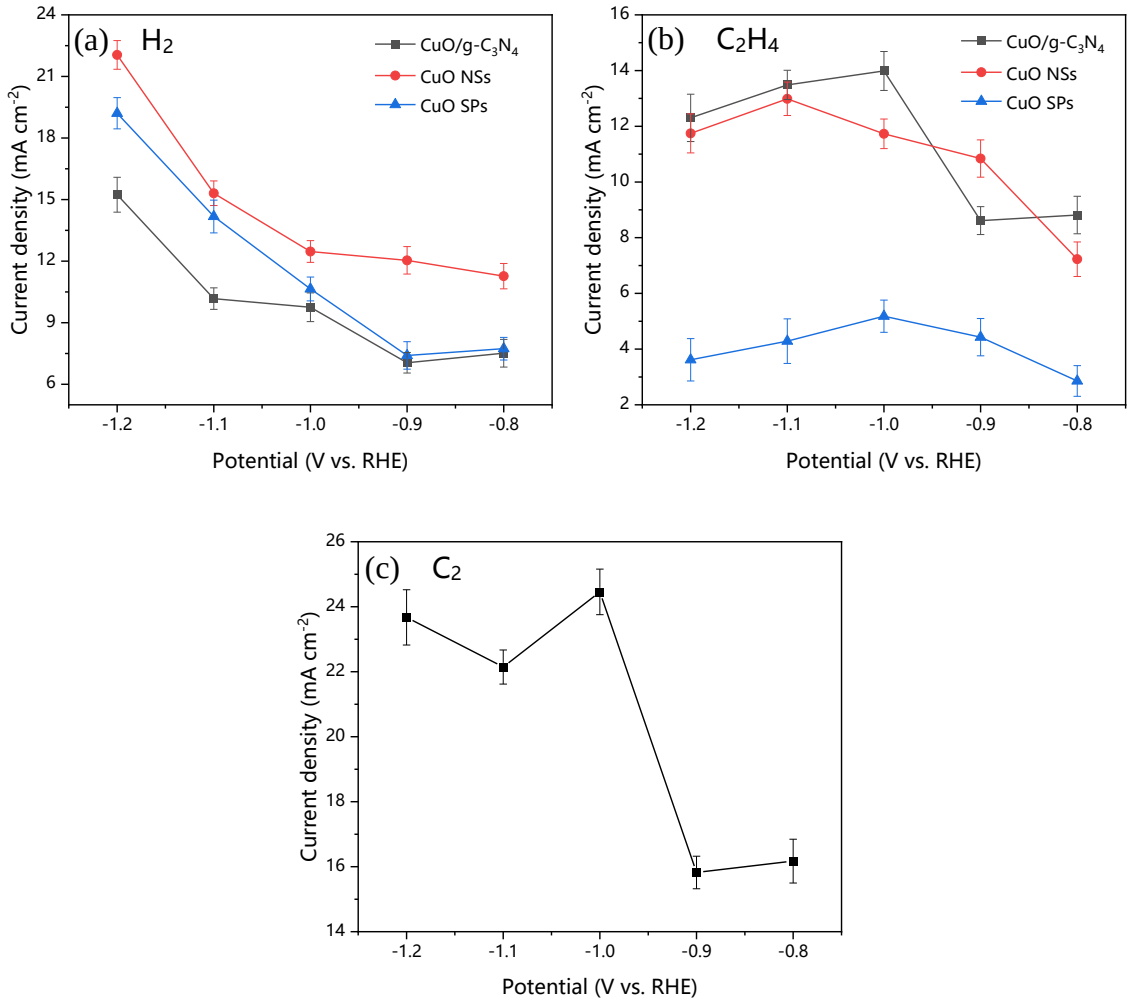

Figure 5.6 Partial current density of the products from CO_2 reductions on each catalyst. (a) H_2, (b) C_2H_4 and (c) C_2 for CuO/g-C_3N_4. Electrolyte: CO_2-saturated 0.1 M $KHCO_3$ solution.

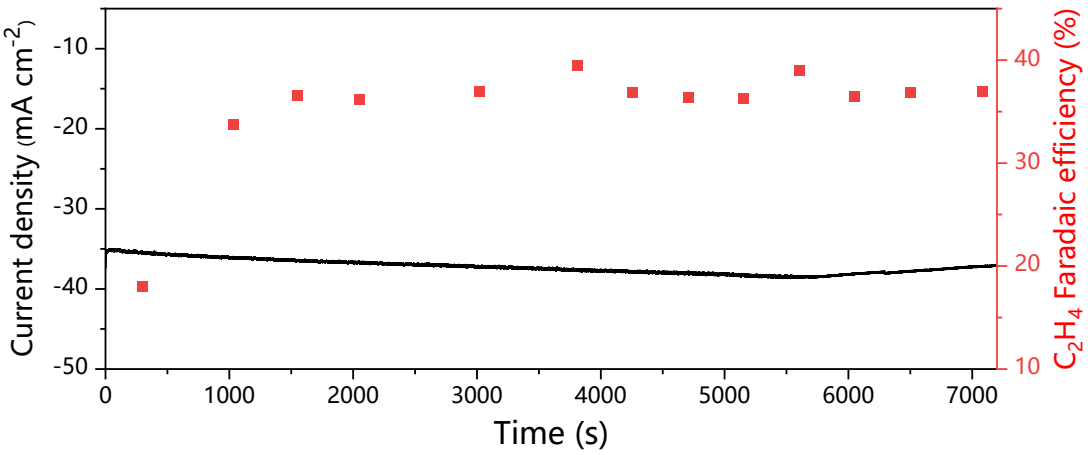

Figure 5.7 Stability test for CuO/g-C_3N_4 at -1.0 V vs. RHE.

Table 5.1 Comparison of various catalysts for CO_2 electroreduction.

Catalyst	Product	Electrolyte	Potential (V vs. RHE)	Faradaic efficiency (%)	Current density (mA cm^{-2})	Ref.
CuO/g-C_3N_4	C_2H_4	0.1 M $KHCO_3$	-1.0	37.0	14.0	This work
	C_2	0.1 M $KHCO_3$	-1.0	64.7	24.5	
Cu NDs	C_2H_4	0.1 M $KHCO_3$	-1.2	22.3	10	(Wu et al., 2020)
HPR-LDH	C_2H_4	0.1 M $KHCO_3$	-1.1	36.0	4.2	(Altaf et al., 2020)
Cu_2O thin films	C_2H_4	0.1 M $KHCO_3$	-0.98	31.0	13.3	(Handoko et al., 2016)
CuZn alloy	C_2H_4	0.1 M $KHCO_3$	-1.1	33.3	2.01	(Feng et al., 2018)
Prism-Cu	C_2H_4	0.1 M $KHCO_3$	-1.15	30	12	(Jeon et al., 2018)
Cu_2O-derived Cu	C_2H_4	0.1 M $KHCO_3$	-0.98	43	13.3	(Handoko et al., 2016)
CuS_2-Cu-V	C_2 & C_{2+}	0.1 M $KHCO_3$	-0.95	23	7.3	(Zhuang et al., 2018)
$Cu_2(OH)Cl$	C_2 & C_{2+}	0.1 M	-1.20	52	31	(De Luna et al.,

		$KHCO_3$				2018)
Cu NPs	C_2 & C_{2+}	0.1 M $KHCO_3$	-0.75	50	10	(Kim et al., 2017)
$Cu(Ag\text{-}20)_{20}$	C_2 & C_{2+}	0.1 M $KHCO_3$	-1.1	31.4	7.9	(Ting et al., 2020)
Cu foil	C_2 & C_{2+}	0.1 M $KHCO_3$	-1.0	60	40	(Jiang et al., 2018b)
Cu_2O-derived particles	C_2 & C_{2+}	0.1 M $KHCO_3$	-1.18	54.4	31.2	(Torelli et al., 2016)
CuX (X = Cl, Br, or I)	C_2 & C_{2+}	0.1 M $KHCO_3$	-1.11	72.6	47.2	(Kim and Palmore, 2020)

CHAPTER VI. CONCLUSION and FUTURE WORK

Electrochemical CO_2R has been challenged by low selectivity for multi-carbon products, difficult suppression of side reactions and poor stability. In order to better improve the performance of CO_2RR, a graphite phase carbon nitride loaded copper oxide composite ($CuO/g\text{-}C_3N_4$) was designed and synthesized to improve the selectivity of electrochemical CO_2R for ethylene and C_2. A series of physicochemical characterization methods were conducted to study morphology and chemical structure composition, following by electrochemical performance study and analysis using electrochemical characterization methods. The main conclusions are as follows. The $CuO/g\text{-}C_3N_4$ composite was synthesized by wet chemically assisted hydrothermal treatment. The structure and morphology of the catalysts were demonstrated by SEM/EDS, TEM, HRTEM, XPS, XRD, FTIR, BET, etc. It was proved that the composite is based on $g\text{-}C_3N_4$ with homogeneous distribution of polycrystalline copper oxide on it. Then, the composite showed a high Faradaic efficiency of 37.0 % for C_2H_4 in 0.1 M $KHCO_3$ electrolyte solution at -1.0 V vs. RHE with a current density of about 14 $mA \cdot cm^{-2}$, which has a significant advantage over pure CuO nanosheets alone (31.7 %, 11.7 $mA \cdot cm^{-2}$) and spherical CuO particles (18.3 %, 5.2 $mA \cdot cm^{-2}$). Meanwhile, the total Faradaic efficiency of the $CuO/g\text{-}C_3N_4$ for C_2 is even 64.7 %, indicating a synergistic promotion between CuO and $g\text{-}C_3N_4$. This work provides an effective strategy to improve the selectivity and activity of C_2 generation by electrocatalytic CO_2 through synergistic effect.

The electroreduction of CO_2 to C_2 and C_{2+} products is an important way to reuse CO_2 and will remain a research area of great interest in the future. The selectivity of CO_2 to a specific C_2 or C_{2+} product is not yet very high and the reaction pathways are not well defined, so there is still a great potential for the development of this field. Based on my literature research and experimental experience on CO_2RR, I have the following perspectives on the research area.

1) The catalytic performance of two-dimensional materials loaded with copper-based catalytic materials needs to be further improved. By changing the preparation process conditions and doping with new metallic or non-metallic elements, the microstructure and composition of the active species are regulated to form large specific surface area, high density and highly active sites to achieve great selectivity for specific products. At the same time, further surface modification, etching, doping of nitrogen-doped carbon containing boron, phosphorus and other groups are needed to explore the catalyst conformational relationships and to lay the foundation for the development of new efficient catalytic materials.

2) Copper-based catalysts are currently the only category which is capable of reducing CO_2 to C_2 and C_{2+} products, and therefore researches related to copper-based catalysts are priority to improve product selectivity. Factors that affect the CO_2R performance of copper-based catalysts include copper valence, morphology, and defect sites, but how each factor affects the CO_2R activity of copper is not very clear. Especially for metal catalysts at the nanoscale, monitoring the atomic and electronic structure changes under actual operating conditions is essential for a better understanding of the active centers and the reaction mechanism. Due to the complexity of the electrode and solid-liquid

interface, the structural characterization of electrocatalysts before and after the reaction is still mainly based on non-in situ characterization. Non-in situ characterization does not adequately characterize the true active sites of the catalysts and can limit the understanding of the reaction mechanism, especially for the complex CO_2RR. Therefore, more in situ characterization tools must be developed for future CO_2R studies. Many researchers have already made significant progress in in situ characterization tools for electrocatalytic systems, such as in situ XAS and quasi-in situ XPS. However, these in situ characterization tools are still not mature enough and have not been widely used in electrocatalyst research.

3) The development of reactors is an important direction for CO_2R research. From the perspective of industrial scale-up, CO_2R not only needs to maintain a high selectivity (> 90%) for specific products, but also needs to maintain a fast reaction generation rate, i.e., to have a large reaction current. However, the conventional H-type reaction cell is limited by the CO_2 mass transfer and its reaction current is generally below 40 mA, which is difficult to meet the scaling-up requirements. Therefore, new types of reactors such as flow cell reactors are gradually attracting the attention of researchers, and their application in CO_2R will further promote the development of the research field.

REFERENCES

ALOTAIBI, B., FAN, S., WANG, D., YE, J. & MI, Z. 2015. Wafer-level artificial photosynthesis for CO2 reduction into CH4 and CO using GaN nanowires. *ACS Catalysis,* 5**,** 5342-5348.

ALTAF, N., LIANG, S., HUANG, L. & WANG, Q. 2020. Electro-derived Cu-Cu_2O nanocluster from LDH for stable and selective C_2 hydrocarbons production from CO_2 electrochemical reduction. *Journal of Energy Chemistry,* 48**,** 169-180.

ATKINS, P. & DE PAULA, J. 2002. *Physical chemistry*, Macmillan.

BAGGER, A., JU, W., VARELA, A. S., STRASSER, P. & ROSSMEISL, J. 2017. Electrochemical CO_2 reduction: a classification problem. *ChemPhysChem,* 18**,** 3266-3273.

BANSODE, A. & URAKAWA, A. 2014. Towards full one-pass conversion of carbon dioxide to methanol and methanol-derived products. *Journal of Catalysis,* 309**,** 66-70.

BASIRATNIA, A., REMPEL, J., LI, F., POGODAEV, A., ZIENCHUK, T. A. & KLINKOVA, A. 2019. Cu (II)-nanoparticle-derived structures under CO 2 reduction conditions: A matter of shape. *Physical Chemistry Chemical Physics,* 21**,** 5894-5897.

BENSON, E. E., KUBIAK, C. P., SATHRUM, A. J. & SMIEJA, J. M. 2009. Electrocatalytic and homogeneous approaches to conversion of CO 2 to liquid fuels. *Chemical Society Reviews,* 38**,** 89-99.

BHATTACHARJEE, A. & AHMARUZZAMAN, M. 2015. Green synthesis of 2D CuO nanoleaves (NLs) and its application for the reduction of p-nitrophenol. *Materials Letters,* 161**,** 79-82.

BIRDJA, Y. Y., SHEN, J. & KOPER, M. T. 2017. Influence of the metal center of metalloprotoporphyrins on the electrocatalytic CO2 reduction to formic acid. *Catalysis Today,* 288**,** 37-47.

BUI, M., ADJIMAN, C. S., BARDOW, A., ANTHONY, E. J., BOSTON, A., BROWN, S., FENNELL, P. S., FUSS, S., GALINDO, A. & HACKETT, L. A. 2018. Carbon capture and storage (CCS): the way forward. *Energy & Environmental Science,* 11**,** 1062-1176.

CAO, S.-W., YUAN, Y.-P., BARBER, J., LOO, S. C. J. & XUE, C. 2014. Noble-metal-free g-C_3N_4/Ni$(dmgH)_2$ composite for efficient photocatalytic hydrogen evolution under visible light irradiation. *Applied surface science,* 319**,** 344-349.

CAWLEY, G. C. 2011. On the atmospheric residence time of anthropogenically sourced carbon dioxide. *Energy & fuels,* 25**,** 5503-5513.

CHEN, C.-S., CHENG, W.-H. & LIN, S.-S. 2003. Study of reverse water gas shift reaction by TPD, TPR and CO2 hydrogenation over potassium-promoted Cu/SiO2 catalyst. *Applied Catalysis A: General,* 238**,** 55-67.

CHEN, Y., LI, C. W. & KANAN, M. W. 2012. Aqueous CO2 reduction at very low overpotential on oxide-derived Au nanoparticles. *Journal of the American Chemical Society,* 134**,** 19969-19972.

CHENG, T., XIAO, H. & GODDARD III, W. A. 2015. Free-energy barriers and reaction mechanisms for the electrochemical reduction of CO on

the Cu (100) surface, including multiple layers of explicit solvent at pH 0. *The journal of physical chemistry letters,* 6**,** 4767-4773.

CHENG, Y., YANG, S., JIANG, S. P. & WANG, S. 2019. Supported single atoms as new class of catalysts for electrochemical reduction of carbon dioxide. *Small Methods,* 3**,** 1800440.

CRIPPA, M., GUIZZARDI, D., MUNTEAN, M., SCHAAF, E., SOLAZZO, E., MONFORTI-FERRARIO, F., OLIVIER, J. & VIGNATI, E. 2020. Fossil CO2 emissions of all world countries. *Luxembourg: European Commission***,** 1-244.

CUI, Y., DING, Z., LIU, P., ANTONIETTI, M., FU, X. & WANG, X. 2012. Metal-free activation of H2O2 by g-C3N4 under visible light irradiation for the degradation of organic pollutants. *Physical Chemistry Chemical Physics,* 14**,** 1455-1462.

DAIYAN, R., LU, X., NG, Y. H. & AMAL, R. 2017. Highly Selective Conversion of CO2 to CO Achieved by a Three‐Dimensional Porous Silver Electrocatalyst. *ChemistrySelect,* 2**,** 879-884.

DAIYAN, R., SAPUTERA, W. H., ZHANG, Q., LOVELL, E., LIM, S., NG, Y. H., LU, X. & AMAL, R. 2019. 3D heterostructured copper electrode for conversion of carbon dioxide to alcohols at low overpotentials. *Advanced Sustainable Systems,* 3**,** 1800064.

DE LUNA, P., QUINTERO-BERMUDEZ, R., DINH, C.-T., ROSS, M. B., BUSHUYEV, O. S., TODOROVIĆ, P., REGIER, T., KELLEY, S. O., YANG, P. & SARGENT, E. H. 2018. Catalyst electro-redeposition controls morphology and oxidation state for selective carbon dioxide reduction. *Nature Catalysis,* 1**,** 103-110.

DUAN, X., XU, J., WEI, Z., MA, J., GUO, S., WANG, S., LIU, H. & DOU, S. 2017. Metal‐free carbon materials for CO2 electrochemical reduction. *Advanced Materials,* 29**,** 1701784.

DUAN, Y. 2018. Facile preparation of CuO/g-C_3N_4 with enhanced photocatalytic degradation of salicylic acid. *Materials Research Bulletin,* 105**,** 68-74.

ELGRISHI, N., ROUNTREE, K. J., MCCARTHY, B. D., ROUNTREE, E. S., EISENHART, T. T. & DEMPSEY, J. L. 2018. A practical beginner's guide to cyclic voltammetry. *Journal of chemical education,* 95**,** 197-206.

FALKOWSKI, P., SCHOLES, R., BOYLE, E., CANADELL, J., CANFIELD, D., ELSER, J., GRUBER, N., HIBBARD, K., HöGBERG, P. & LINDER, S. 2000. The global carbon cycle: a test of our knowledge of earth as a system. *Science,* 290**,** 291-296.

FENG, X., JIANG, K., FAN, S. & KANAN, M. W. 2015. Grain-boundary-dependent CO2 electroreduction activity. *Journal of the American Chemical Society,* 137**,** 4606-4609.

FENG, X., JIANG, K., FAN, S. & KANAN, M. W. 2016. A direct grain-boundary-activity correlation for CO electroreduction on Cu nanoparticles. *ACS central science,* 2**,** 169-174.

FENG, Y., LI, Z., LIU, H., DONG, C., WANG, J., KULINICH, S. A. & DU, X. 2018. Laser-prepared CuZn alloy catalyst for selective electrochemical reduction of CO_2 to ethylene. *Langmuir,* 34**,** 13544-13549.

FU, J., JIANG, K., QIU, X., YU, J. & LIU, M. 2020. Product selectivity of photocatalytic CO_2 reduction reactions. *Materials Today,* 32**,** 222-243.

FU, J., YU, J., JIANG, C. & CHENG, B. 2018a. g‐C3N4‐Based heterostructured photocatalysts. *Advanced Energy Materials,* 8**,** 1701503.

FU, S., LIU, X., RAN, J., JIAO, Y. & QIAO, S.-Z. 2021. CO2 reduction by single copper atom supported on g-C3N4 with asymmetrical active sites. *Applied Surface Science,* 540**,** 148293.

FU, Y., ZHU, C., WANG, H., DOU, Y., SHI, W., SHAO, M., HUANG, H., LIU, Y. & KANG, Z. 2018b. High-performance NiO/g-C_3N_4 composites for visible-light-driven photocatalytic overall water splitting. *Inorganic Chemistry Frontiers,* 5**,** 1646-1652.

GILLAN, E. G. 2000. Synthesis of nitrogen-rich carbon nitride networks from an energetic molecular azide precursor. *Chemistry of materials,* 12**,** 3906-3912.

GOEPPERT, A., CZAUN, M., PRAKASH, G. S. & OLAH, G. A. 2012. Air as the renewable carbon source of the future: an overview of CO 2 capture from the atmosphere. *Energy & Environmental Science,* 5**,** 7833-7853.

GOGLIO, G., FOY, D. & DEMAZEAU, G. 2008. State of Art and recent trends in bulk carbon nitrides synthesis. *Materials Science and Engineering: R: Reports,* 58**,** 195-227.

GREENWOOD, N. N. & EARNSHAW, A. 2012. *Chemistry of the Elements,* Elsevier.

GU, J., HéROGUEL, F., LUTERBACHER, J. & HU, X. 2018. Densely packed, ultra small SnO nanoparticles for enhanced activity and selectivity in electrochemical CO2 reduction. *Angewandte Chemie,* 130**,** 2993-2997.

HAN, C., SU, P., TAN, B., MA, X., LV, H., HUANG, C., WANG, P., TONG, Z., LI, G. & HUANG, Y. 2021. Defective ultra-thin two-dimensional g-C3N4 photocatalyst for enhanced photocatalytic H2 evolution activity. *Journal of Colloid and Interface Science,* 581**,** 159-166.

HANDOKO, A. D., ONG, C. W., HUANG, Y., LEE, Z. G., LIN, L., PANETTI, G. B. & YEO, B. S. 2016. Mechanistic insights into the selective electroreduction of carbon dioxide to ethylene on Cu_2O-derived copper catalysts. *The Journal of Physical Chemistry C,* 120**,** 20058-20067.

HOANG, T. T., VERMA, S., MA, S., FISTER, T. T., TIMOSHENKO, J., FRENKEL, A. I., KENIS, P. J. & GEWIRTH, A. A. 2018. Nanoporous copper–silver alloys by additive-controlled electrodeposition for the selective electroreduction of CO2 to ethylene and ethanol. *Journal of the American Chemical Society,* 140**,** 5791-5797.

HORI, Y., KIKUCHI, K., MURATA, A. & SUZUKI, S. 1986. Production of methane and ethylene in electrochemical reduction of carbon dioxide at copper electrode in aqueous hydrogencarbonate solution. *Chemistry Letters,* 15**,** 897-898.

HORI, Y., MURATA, A. & TAKAHASHI, R. 1989. Formation of hydrocarbons in the electrochemical reduction of carbon dioxide at a copper electrode in aqueous solution. *Journal of the Chemical Society, Faraday Transactions 1: Physical Chemistry in Condensed Phases,* 85**,** 2309-2326.

HORI, Y., MURATA, A., TAKAHASHI, R. & SUZUKI, S. 1988. Enhanced formation of ethylene and alcohols at ambient temperature and pressure in electrochemical reduction of carbon dioxide at a copper electrode. *Journal of the Chemical Society, Chemical Communications***,** 17-19.

HORI, Y., TAKAHASHI, I., KOGA, O. & HOSHI, N. 2002. Selective formation of C2 compounds from electrochemical reduction of CO2 at a series of copper single crystal electrodes. *The Journal of Physical Chemistry B,* 106**,** 15-17.

HORI, Y., TAKAHASHI, I., KOGA, O. & HOSHI, N. 2003. Electrochemical reduction of carbon dioxide at various series of copper single crystal electrodes. *Journal of Molecular Catalysis A: Chemical,* 199**,** 39-47.

HORI, Y., TAKAHASHI, R., YOSHINAMI, Y. & MURATA, A. 1997. Electrochemical reduction of CO at a copper electrode. *The Journal of Physical Chemistry B,* 101**,** 7075-7081.

HORI, Y., WAKEBE, H., TSUKAMOTO, T. & KOGA, O. 1994. Electrocatalytic process of CO selectivity in electrochemical reduction of CO2 at metal electrodes in aqueous media. *Electrochimica Acta,* 39**,** 1833-1839.

HU, C., ZANG, G.-L., LUO, J.-T., LIU, Q. & ZHAO, Q. 2021. A novel spherical-ordered macroporous CuO nanocatalyst for the electrochemical reduction of carbon dioxide. *Journal of Applied Electrochemistry,* 51**,** 847-859.

HUANG, H., YANG, S., VAJTAI, R., WANG, X. & AJAYAN, P. M. 2014. Pt‐decorated 3D architectures built from graphene and graphitic carbon nitride nanosheets as efficient methanol oxidation catalysts. *Advanced Materials,* 26**,** 5160-5165.

HUANG, J., GUO, X., HUANG, X. & WANG, L. 2019. Metal (Sn, Bi, Pb, Cd) in-situ anchored on mesoporous hollow kapok-tubes for outstanding electrocatalytic CO2 reduction to formate. *Electrochimica Acta,* 325**,** 134923.

JEON, H. S., KUNZE, S., SCHOLTEN, F. & ROLDAN CUENYA, B. 2018. Prism-shaped Cu nanocatalysts for electrochemical CO_2 reduction to ethylene. *ACS Catalysis,* 8**,** 531-535.

JIANG, B., ZHANG, X.-G., JIANG, K., WU, D.-Y. & CAI, W.-B. 2018a. Boosting formate production in electrocatalytic CO2 reduction over wide potential window on Pd surfaces. *Journal of the American Chemical Society,* 140**,** 2880-2889.

JIANG, K., SANDBERG, R. B., AKEY, A. J., LIU, X., BELL, D. C., NøRSKOV, J. K., CHAN, K. & WANG, H. 2018b. Metal ion cycling of Cu foil for selective C–C coupling in electrochemical CO_2 reduction. *Nature Catalysis,* 1**,** 111-119.

JIAO, Y., ZHENG, Y., CHEN, P., JARONIEC, M. & QIAO, S.-Z. 2017. Molecular scaffolding strategy with synergistic active centers to facilitate electrocatalytic CO_2 reduction to hydrocarbon/alcohol. *Journal of the American Chemical Society,* 139**,** 18093-18100.

JUN, Y. S., LEE, E. Z., WANG, X., HONG, W. H., STUCKY, G. D. & THOMAS, A. 2013. From melamine‐cyanuric acid supramolecular aggregates to carbon nitride hollow spheres. *Advanced Functional Materials,* 23**,** 3661-3667.

JUNG, H., LEE, S. Y., LEE, C. W., CHO, M. K., WON, D. H., KIM, C., OH, H.-S., MIN, B. K. & HWANG, Y. J. 2019. Electrochemical fragmentation of Cu2O nanoparticles enhancing selective C–C coupling from CO2 reduction reaction. *Journal of the American Chemical Society,* 141**,** 4624-4633.

KE, F.-S., LIU, X.-C., WU, J., SHARMA, P. P., ZHOU, Z.-Y., QIAO, J. & ZHOU, X.-D. 2017. Selective formation of C2 products from the electrochemical conversion of CO2 on CuO-derived copper electrodes comprised of nanoporous ribbon arrays. *Catalysis Today,* 288**,** 18-23.

KIM, D., KLEY, C. S., LI, Y. & YANG, P. 2017. Copper nanoparticle ensembles for selective electroreduction of CO_2 to C_2–C_3 products. *Proceedings of the National Academy of Sciences,* 114**,** 10560-10565.

KIM, D., RESASCO, J., YU, Y., ASIRI, A. M. & YANG, P. 2014. Synergistic geometric and electronic effects for electrochemical reduction of carbon dioxide using gold–copper bimetallic nanoparticles. *Nature communications,* 5**,** 1-8.

KIM, J., CHOI, W., PARK, J. W., KIM, C., KIM, M. & SONG, H. 2019. Branched copper oxide nanoparticles induce highly selective ethylene production by electrochemical carbon dioxide reduction. *Journal of the American Chemical Society,* 141**,** 6986-6994.

KIM, T. & PALMORE, G. T. R. 2020. A scalable method for preparing Cu electrocatalysts that convert CO_2 into C_{2+} products. *Nature communications,* 11**,** 1-11.

KLICHE, G. & POPOVIC, Z. 1990. Far-infrared spectroscopic investigations on CuO. *Physical Review B,* 42**,** 10060.

KOHL, W. L. 2010. Consumer country energy cooperation: The International Energy Agency and the global energy order. *Global energy governance: The new rules of the game***,** 195-220.

KONDRATENKO, E. V., MUL, G., BALTRUSAITIS, J., LARRAZáBAL, G. O. & PéREZ-RAMíREZ, J. 2013. Status and perspectives of CO_2 conversion into fuels and chemicals by catalytic, photocatalytic and electrocatalytic processes. *Energy & Environmental Science,* 6**,** 3112-3135.

KORTLEVER, R., SHEN, J., SCHOUTEN, K. J. P., CALLE-VALLEJO, F. & KOPER, M. T. 2015. Catalysts and reaction pathways for the electrochemical reduction of carbon dioxide. *The journal of physical chemistry letters,* 6**,** 4073-4082.

KROKE, E., SCHWARZ, M., HORATH-BORDON, E., KROLL, P., NOLL, B. & NORMAN, A. D. 2002. Tri-s-triazine derivatives. Part I. From trichloro-tri-s-triazine to graphitic C 3 N 4 structures. *New Journal of Chemistry,* 26**,** 508-512.

KUHL, K. P., CAVE, E. R., ABRAM, D. N. & JARAMILLO, T. F. 2012. New insights into the electrochemical reduction of carbon dioxide on metallic copper surfaces. *Energy & Environmental Science,* 5**,** 7050-7059.

KUMAR, P., BOUKHERROUB, R. & SHANKAR, K. 2018. Sunlight-driven water-splitting using two-dimensional carbon based semiconductors. *Journal of Materials Chemistry A,* 6**,** 12876-12931.

LEE, C. W., YANG, K. D., NAM, D. H., JANG, J. H., CHO, N. H., IM, S. W. & NAM, K. T. 2018. Defining a materials database for the design of

copper binary alloy catalysts for electrochemical CO2 conversion. *Advanced Materials,* 30**,** 1704717.

LEE, S., PARK, G. & LEE, J. 2017. Importance of Ag–Cu biphasic boundaries for selective electrochemical reduction of CO2 to ethanol. *Acs Catalysis,* 7**,** 8594-8604.

LI, C. W., CISTON, J. & KANAN, M. W. 2014a. Electroreduction of carbon monoxide to liquid fuel on oxide-derived nanocrystalline copper. *Nature,* 508**,** 504-507.

LI, H., LI, Y., KOPER, M. T. & CALLE-VALLEJO, F. 2014b. Bond-making and breaking between carbon, nitrogen, and oxygen in electrocatalysis. *Journal of the American Chemical Society,* 136**,** 15694-15701.

LI, K., PENG, B. & PENG, T. 2016a. Recent advances in heterogeneous photocatalytic CO2 conversion to solar fuels. *ACS Catalysis,* 6**,** 7485-7527.

LI, M., WANG, J., LI, P., CHANG, K., LI, C., WANG, T., JIANG, B., ZHANG, H., LIU, H. & YAMAUCHI, Y. 2016b. Mesoporous palladium–copper bimetallic electrodes for selective electrocatalytic reduction of aqueous CO 2 to CO. *Journal of Materials Chemistry A,* 4**,** 4776-4782.

LI, X., WANG, Y., TIAN, W. & CAO, J. 2019. Graphitic carbon nitride nanosheets decorated flower-like NiO composites for high-performance triethylamine detection. *ACS omega,* 4**,** 9645-9653.

LI, Y., CUI, F., ROSS, M. B., KIM, D., SUN, Y. & YANG, P. 2017. Structure-sensitive CO2 electroreduction to hydrocarbons on ultrathin 5-fold twinned copper nanowires. *Nano letters,* 17**,** 1312-1317.

LI, Y., ZHANG, J., WANG, Q., JIN, Y., HUANG, D., CUI, Q. & ZOU, G. 2010. Nitrogen-rich carbon nitride hollow vessels: synthesis, characterization, and their properties. *The Journal of Physical Chemistry B,* 114**,** 9429-9434.

LIU, A. Y. & COHEN, M. L. 1989. Prediction of new low compressibility solids. *Science,* 245**,** 841-842.

LIU, E., LIN, X., HONG, Y., YANG, L., LUO, B., SHI, W. & SHI, J. 2021. Rational copolymerization strategy engineered C self-doped g-C3N4 for efficient and robust solar photocatalytic H2 evolution. *Renewable Energy,* 178**,** 757-765.

LIU, H., ZHU, Y., MA, J., ZHANG, Z. & HU, W. 2020. Recent advances in atomic - level engineering of nanostructured catalysts for electrochemical CO_2 reduction. *Advanced Functional Materials,* 30**,** 1910534.

LIU, X., SCHLEXER, P., XIAO, J., JI, Y., WANG, L., SANDBERG, R. B., TANG, M., BROWN, K. S., PENG, H. & RINGE, S. 2019. pH effects on the electrochemical reduction of CO (2) towards C2 products on stepped copper. *Nature communications,* 10**,** 1-10.

LOIUDICE, A., LOBACCARO, P., KAMALI, E. A., THAO, T., HUANG, B. H., AGER, J. W. & BUONSANTI, R. 2016. Tailoring copper nanocrystals towards C2 products in electrochemical CO2 reduction. *Angewandte Chemie International Edition,* 55**,** 5789-5792.

LU, L., WANG, B., WANG, S., SHI, Z., YAN, S. & ZOU, Z. 2017. La2O3-Modified LaTiO2N Photocatalyst with Spatially Separated Active Sites

Achieving Enhanced CO2 Reduction. *Advanced Functional Materials,* 27**,** 1702447.

LUM, Y. & AGER, J. W. 2018a. Sequential catalysis controls selectivity in electrochemical CO 2 reduction on Cu. *Energy & Environmental Science,* 11**,** 2935-2944.

LUM, Y. & AGER, J. W. 2018b. Stability of residual oxides in oxide‐derived copper catalysts for electrochemical CO_2 reduction investigated with ^{18}O labeling. *Angewandte Chemie International Edition,* 57**,** 551-554.

LUM, Y., YUE, B., LOBACCARO, P., BELL, A. T. & AGER, J. W. 2017. Optimizing C–C coupling on oxide-derived copper catalysts for electrochemical CO2 reduction. *The Journal of Physical Chemistry C,* 121**,** 14191-14203.

MA, S., SADAKIYO, M., HEIMA, M., LUO, R., HAASCH, R. T., GOLD, J. I., YAMAUCHI, M. & KENIS, P. J. 2017. Electroreduction of carbon dioxide to hydrocarbons using bimetallic Cu–Pd catalysts with different mixing patterns. *Journal of the American Chemical Society,* 139**,** 47-50.

MANDAL, L., YANG, K. R., MOTAPOTHULA, M. R., REN, D., LOBACCARO, P., PATRA, A., SHERBURNE, M., BATISTA, V. S., YEO, B. S. & AGER, J. W. 2018. Investigating the role of copper oxide in electrochemical CO2 reduction in real time. *ACS applied materials & interfaces,* 10**,** 8574-8584.

MAO, Z., CHEN, J., YANG, Y., WANG, D., BIE, L. & FAHLMAN, B. D. 2017. Novel g-C_3N_4/CoO nanocomposites with significantly enhanced visible-light photocatalytic activity for H_2 evolution. *ACS applied materials & interfaces,* 9**,** 12427-12435.

MENG, A., ZHANG, L., CHENG, B. & YU, J. 2018. TiO2–MnO x–Pt hybrid multiheterojunction film photocatalyst with enhanced photocatalytic CO2-reduction activity. *ACS applied materials & interfaces,* 11**,** 5581-5589.

MISTRY, H., VARELA, A. S., BONIFACIO, C. S., ZEGKINOGLOU, I., SINEV, I., CHOI, Y.-W., KISSLINGER, K., STACH, E. A., YANG, J. C. & STRASSER, P. 2016. Highly selective plasma-activated copper catalysts for carbon dioxide reduction to ethylene. *Nature communications,* 7**,** 1-9.

MONTOYA, J. H., SHI, C., CHAN, K. & NøRSKOV, J. K. 2015. Theoretical insights into a CO dimerization mechanism in CO2 electroreduction. *The journal of physical chemistry letters,* 6**,** 2032-2037.

NIELSEN, D. U., HU, X.-M., DAASBJERG, K. & SKRYDSTRUP, T. 2018. Chemically and electrochemically catalysed conversion of CO_2 to CO with follow-up utilization to value-added chemicals. *Nature Catalysis,* 1**,** 244-254.

NITOPI, S., BERTHEUSSEN, E., SCOTT, S. B., LIU, X., ENGSTFELD, A. K., HORCH, S., SEGER, B., STEPHENS, I. E. L., CHAN, K., HAHN, C., NøRSKOV, J. K., JARAMILLO, T. F. & CHORKENDORFF, I. 2019. Progress and Perspectives of Electrochemical CO_2 Reduction on Copper in Aqueous Electrolyte. *Chemical Reviews,* 119**,** 7610-7672.

NIU, P., YANG, Y., JIMMY, C. Y., LIU, G. & CHENG, H.-M. 2014. Switching the selectivity of the photoreduction reaction of carbon

dioxide by controlling the band structure of a gC 3 N 4 photocatalyst. *Chemical Communications,* 50**,** 10837-10840.

OLAH, G. A., PRAKASH, G. S. & GOEPPERT, A. 2011. Anthropogenic chemical carbon cycle for a sustainable future. *Journal of the American Chemical Society,* 133**,** 12881-12898.

ONG, W.-J., TAN, L.-L., NG, Y. H., YONG, S.-T. & CHAI, S.-P. 2016. Graphitic carbon nitride (g-C3N4)-based photocatalysts for artificial photosynthesis and environmental remediation: are we a step closer to achieving sustainability? *Chemical reviews,* 116**,** 7159-7329.

ORR JR, F. M. 2009. CO 2 capture and storage: are we ready? *Energy & Environmental Science,* 2**,** 449-458.

PETERSON, A. A., ABILD-PEDERSEN, F., STUDT, F., ROSSMEISL, J. & NøRSKOV, J. K. 2010. How copper catalyzes the electroreduction of carbon dioxide into hydrocarbon fuels. *Energy & Environmental Science,* 3**,** 1311-1315.

PIRES, J., MARTINS, F., ALVIM-FERRAZ, M. & SIMõES, M. 2011. Recent developments on carbon capture and storage: An overview. *Chemical engineering research and design,* 89**,** 1446-1460.

PROIETTO, F., SCHIAVO, B., GALIA, A. & SCIALDONE, O. 2018. Electrochemical conversion of CO2 to HCOOH at tin cathode in a pressurized undivided filter-press cell. *Electrochimica Acta,* 277**,** 30-40.

REDEMANN, C. & LUCAS, H. 1940. Some derivatives of cyameluric acid and probable structures of melam, melem and melon. *Journal of the American Chemical Society,* 62**,** 842-846.

REN, D., ANG, B. S.-H. & YEO, B. S. 2016. Tuning the selectivity of carbon dioxide electroreduction toward ethanol on oxide-derived Cu x Zn catalysts. *Acs Catalysis,* 6**,** 8239-8247.

RESKE, R., MISTRY, H., BEHAFARID, F., ROLDAN CUENYA, B. & STRASSER, P. 2014. Particle size effects in the catalytic electroreduction of CO2 on Cu nanoparticles. *Journal of the American Chemical Society,* 136**,** 6978-6986.

ROGELJ, J., HUPPMANN, D., KREY, V., RIAHI, K., CLARKE, L., GIDDEN, M., NICHOLLS, Z. & MEINSHAUSEN, M. 2019. A new scenario logic for the Paris Agreement long-term temperature goal. *Nature,* 573**,** 357-363.

ROSEN, J., HUTCHINGS, G. S., LU, Q., FOREST, R. V., MOORE, A. & JIAO, F. 2015. Electrodeposited Zn dendrites with enhanced CO selectivity for electrocatalytic CO2 reduction. *Acs Catalysis,* 5**,** 4586-4591.

SANDBERG, R. B., MONTOYA, J. H., CHAN, K. & NøRSKOV, J. K. 2016. CO-CO coupling on Cu facets: Coverage, strain and field effects. *Surface Science,* 654**,** 56-62.

SARFRAZ, S., GARCIA-ESPARZA, A. T., JEDIDI, A., CAVALLO, L. & TAKANABE, K. 2016. Cu–Sn bimetallic catalyst for selective aqueous electroreduction of CO2 to CO. *ACS Catalysis,* 6**,** 2842-2851.

SCHOLTEN, F., SINEV, I., BERNAL, M. & ROLDAN CUENYA, B. 2019. Plasma-modified dendritic Cu catalyst for CO_2 electroreduction. *ACS catalysis,* 9**,** 5496-5502.

SCHOUTEN, K. J. P., QIN, Z., PÉREZ GALLENT, E. & KOPER, M. T. 2012. Two pathways for the formation of ethylene in CO reduction on

single-crystal copper electrodes. *Journal of the American Chemical Society,* 134**,** 9864-9867.

SIEGELMAN, R. L., MILNER, P. J., KIM, E. J., WESTON, S. C. & LONG, J. R. 2019. Challenges and opportunities for adsorption-based CO 2 capture from natural gas combined cycle emissions. *Energy & environmental science,* 12**,** 2161-2173.

SUMMERS, D. & FRESE, K. 1988. The electrochemical reduction of aqueous carbon monoxide and methanol to methane at ruthenium electrodes. *Journal of the Electrochemical Society,* 135**,** 264.

SUN, Q., LV, K., ZHANG, Z., LI, M. & LI, B. 2015. Effect of contact interface between TiO_2 and g-C_3N_4 on the photoreactivity of g-C_3N_4/TiO_2 photocatalyst: (0 0 1) vs (1 0 1) facets of TiO_2. *Applied Catalysis B: Environmental,* 164**,** 420-427.

TEETER, T. E. & VAN RYSSELBERGHE, P. 1954. Reduction of carbon dioxide on mercury cathodes. *The Journal of Chemical Physics,* 22**,** 759-760.

TETER, D. M. & HEMLEY, R. J. 1996. Low-compressibility carbon nitrides. *Science,* 271**,** 53-55.

TING, L. R. L., PIQUE, O., LIM, S. Y., TANHAEI, M., CALLE-VALLEJO, F. & YEO, B. S. 2020. Enhancing CO_2 electroreduction to ethanol on copper–silver composites by opening an alternative catalytic pathway. *ACS Catalysis,* 10**,** 4059-4069.

TORELLI, D. A., FRANCIS, S. A., CROMPTON, J. C., JAVIER, A., THOMPSON, J. R., BRUNSCHWIG, B. S., SORIAGA, M. P. & LEWIS, N. S. 2016. Nickel–gallium-catalyzed electrochemical reduction of CO_2 to highly reduced products at low overpotentials. *ACS catalysis,* 6**,** 2100-2104.

TRINDELL, J. A., CLAUSMEYER, J. & CROOKS, R. M. 2017. Size stability and H2/CO selectivity for Au nanoparticles during electrocatalytic CO2 reduction. *Journal of the American Chemical Society,* 139**,** 16161-16167.

WANG, X., MAEDA, K., THOMAS, A., TAKANABE, K., XIN, G., CARLSSON, J. M., DOMEN, K. & ANTONIETTI, M. 2009. A metal-free polymeric photocatalyst for hydrogen production from water under visible light. *Nature materials,* 8**,** 76-80.

WANG, Y., GAO, B., YUE, Q. & WANG, Z. 2020a. Graphitic carbon nitride (gC 3 N 4)-based membranes for advanced separation. *Journal of Materials Chemistry A,* 8**,** 19133-19155.

WANG, Y., WANG, X. & ANTONIETTI, M. 2012. Polymeric graphitic carbon nitride as a heterogeneous organocatalyst: from photochemistry to multipurpose catalysis to sustainable chemistry. *Angewandte Chemie International Edition,* 51**,** 68-89.

WANG, Y., WANG, Z., DINH, C.-T., LI, J., OZDEN, A., GOLAM KIBRIA, M., SEIFITOKALDANI, A., TAN, C.-S., GABARDO, C. M. & LUO, M. 2020b. Catalyst synthesis under CO2 electroreduction favours faceting and promotes renewable fuels electrosynthesis. *Nature Catalysis,* 3**,** 98-106.

WU, M., ZHU, C., WANG, K., LI, G., DONG, X., SONG, Y., XUE, J., CHEN, W., WEI, W. & SUN, Y. 2020. Promotion of CO_2 electrochemical

reduction via Cu nanodendrites. *ACS applied materials & interfaces,* 12**,** 11562-11569.

XIA, Z., FREEMAN, M., ZHANG, D., YANG, B., LEI, L., LI, Z. & HOU, Y. 2018. Highly selective electrochemical conversion of CO2 to HCOOH on dendritic indium foams. *ChemElectroChem,* 5**,** 253-259.

XIAO, H., GODDARD III, W. A., CHENG, T. & LIU, Y. 2017. Cu metal embedded in oxidized matrix catalyst to promote CO2 activation and CO dimerization for electrochemical reduction of CO2. *Proceedings of the National Academy of Sciences,* 114**,** 6685-6688.

YAN, S., LI, Z. & ZOU, Z. 2009. Photodegradation performance of g-C3N4 fabricated by directly heating melamine. *Langmuir,* 25**,** 10397-10401.

YU, S., WILSON, A. J., HEO, J. & JAIN, P. K. 2018. Plasmonic control of multi-electron transfer and C–C coupling in visible-light-driven CO2 reduction on Au nanoparticles. *Nano letters,* 18**,** 2189-2194.

ZHANG, J., CHEN, X., TAKANABE, K., MAEDA, K., DOMEN, K., EPPING, J. D., FU, X., ANTONIETTI, M. & WANG, X. 2010. Synthesis of a carbon nitride structure for visible‐light catalysis by copolymerization. *Angewandte Chemie International Edition,* 49**,** 441-444.

ZHANG, L., ZHAO, Z. J. & GONG, J. 2017. Nanostructured materials for heterogeneous electrocatalytic CO2 reduction and their related reaction mechanisms. *Angewandte Chemie International Edition,* 56**,** 11326-11353.

ZHANG, W., HU, Y., MA, L., ZHU, G., WANG, Y., XUE, X., CHEN, R., YANG, S. & JIN, Z. 2018a. Progress and perspective of electrocatalytic CO2 reduction for renewable carbonaceous fuels and chemicals. *Advanced Science,* 5**,** 1700275.

ZHANG, W., HU, Y., MA, L., ZHU, G., ZHAO, P., XUE, X., CHEN, R., YANG, S., MA, J. & LIU, J. 2018b. Liquid-phase exfoliated ultrathin Bi nanosheets: uncovering the origins of enhanced electrocatalytic CO2 reduction on two-dimensional metal nanostructure. *Nano Energy,* 53**,** 808-816.

ZHANG, Y., SHI, J., HUANG, Z., GUAN, X., ZONG, S., CHENG, C., ZHENG, B. & GUO, L. 2020. Synchronous construction of CoS2 in-situ loading and S doping for g-C3N4: enhanced photocatalytic H2-evolution activity and mechanism insight. *Chemical Engineering Journal,* 401**,** 126135.

ZHAO, L., KUANG, X., LIU, Z., HOU, Y., WANG, Z., WEI, Q., LEE, J. Y. & KANG, B. 2019. Anchoring CuO nanoparticles on C, N‐codoped G‐C_3N_4 nanosheets from melamine‐entrapped MOF gel for high‐efficiency oxygen evolution. *ChemNanoMat,* 5**,** 1170-1175.

ZHAO, S., JIN, R. & JIN, R. 2018a. Opportunities and challenges in CO2 reduction by gold-and silver-based electrocatalysts: from bulk metals to nanoparticles and atomically precise nanoclusters. *ACS energy letters,* 3**,** 452-462.

ZHAO, S., TANG, Z., GUO, S., HAN, M., ZHU, C., ZHOU, Y., BAI, L., GAO, J., HUANG, H. & LI, Y. 2018b. Enhanced activity for CO_2

electroreduction on a highly active and stable ternary Au-CDots-C_3N_4 electrocatalyst. *ACS Catalysis,* 8**,** 188-197.

ZHENG, L. & LIU, X. 2007. Solution-phase synthesis of CuO hierarchical nanosheets at near-neutral pH and near-room temperature. *Materials Letters,* 61**,** 2222-2226.

ZHENG, Y., JIAO, Y., ZHU, Y., CAI, Q., VASILEFF, A., LI, L. H., HAN, Y., CHEN, Y. & QIAO, S.-Z. 2017. Molecule-level g-C3N4 coordinated transition metals as a new class of electrocatalysts for oxygen electrode reactions. *Journal of the American Chemical Society,* 139**,** 3336-3339.

ZHUANG, T.-T., LIANG, Z.-Q., SEIFITOKALDANI, A., LI, Y., DE LUNA, P., BURDYNY, T., CHE, F., MENG, F., MIN, Y. & QUINTERO-BERMUDEZ, R. 2018. Steering post-C–C coupling selectivity enables high efficiency electroreduction of carbon dioxide to multi-carbon alcohols. *Nature Catalysis,* 1**,** 421-428.

ZOU, X., SU, J., SILVA, R., GOSWAMI, A., SATHE, B. R. & ASEFA, T. 2013. Efficient oxygen evolution reaction catalyzed by low-density Ni-doped Co 3 O 4 nanomaterials derived from metal-embedded graphitic C 3 N 4. *Chemical Communications,* 49**,** 7522-7524.

APPENDIX

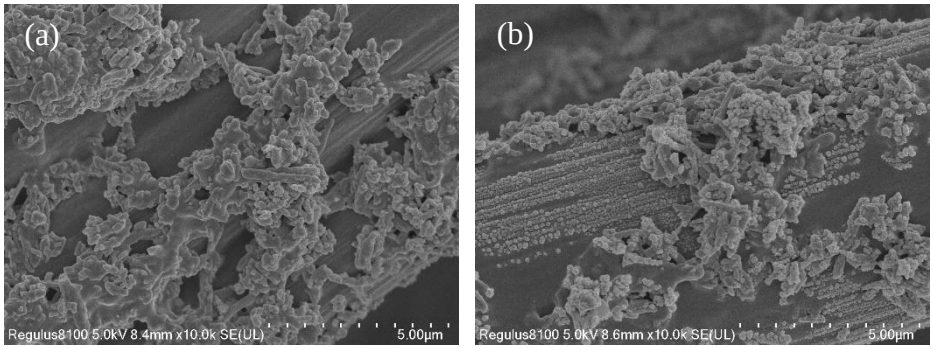

Figure S1. CuO NSs loaded on carbon paper (a) before reaction and (b) after 2 h reaction.

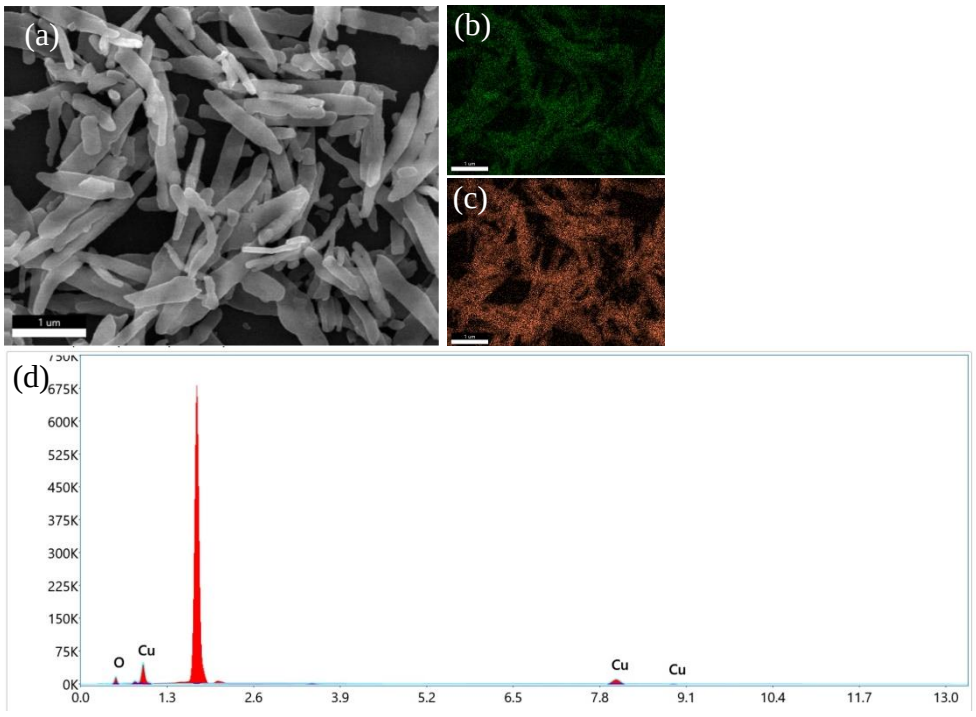

Figure S2. (a) SEM image, and elemental mapping of (b) O, (c) Cu, and (d) EDS spectroscopy of CuO NSs.

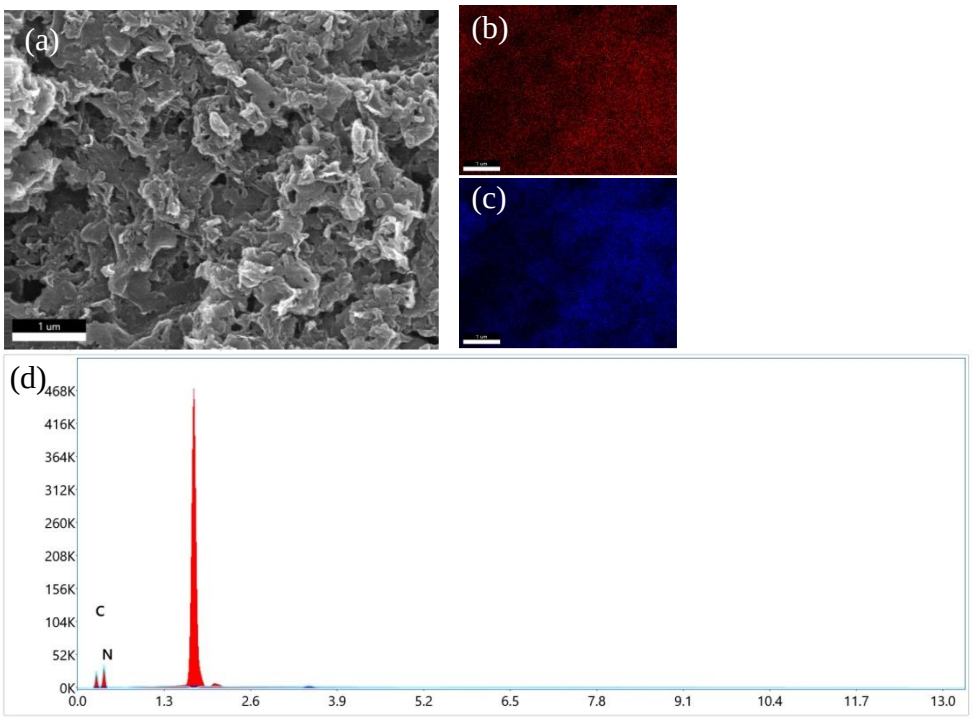

Figure S3. (a) SEM image, and elemental mapping of (b) C, (c) N, and (d) EDS spectroscopy of g-C_3N_4.

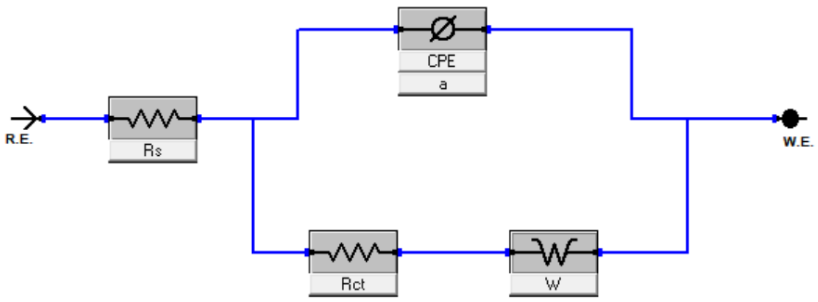

Figure S4. EIS equivalent circuit of CuO SPs, CuO NSs and CuO/g-C_3N_4 in CO_2-saturated $KHCO_3$ solution.

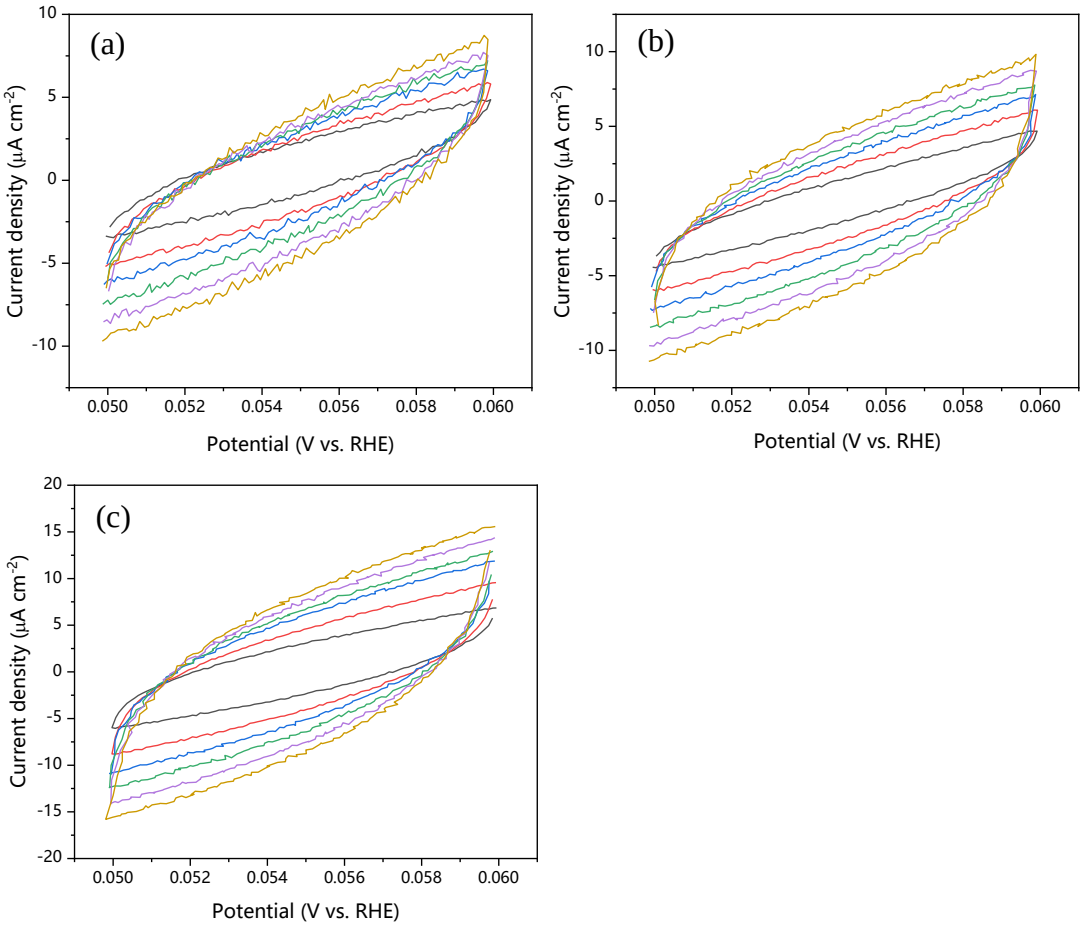

Figure S5. CVs of (a) CuO SPs, (b) CuO NSs and (c) CuO/g-C_3N_4 electrodes at different scan rates (20 ~ 120 mV·s^{-1}) in the potential range of 50 ~ 60 mV vs. RHE.

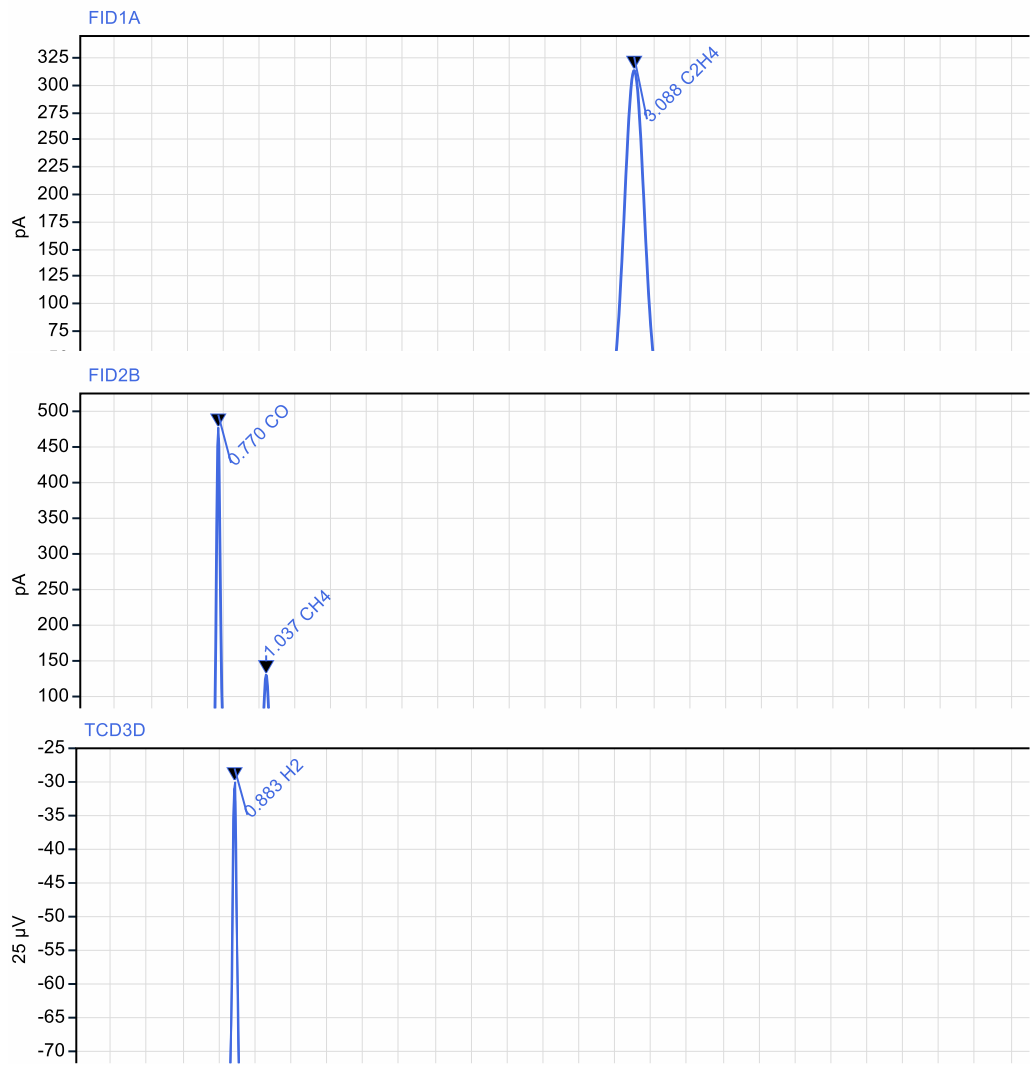

Figure S6. Representative GC-FID and GC-TCD chromatograms of CuO/g-C_3N_4.

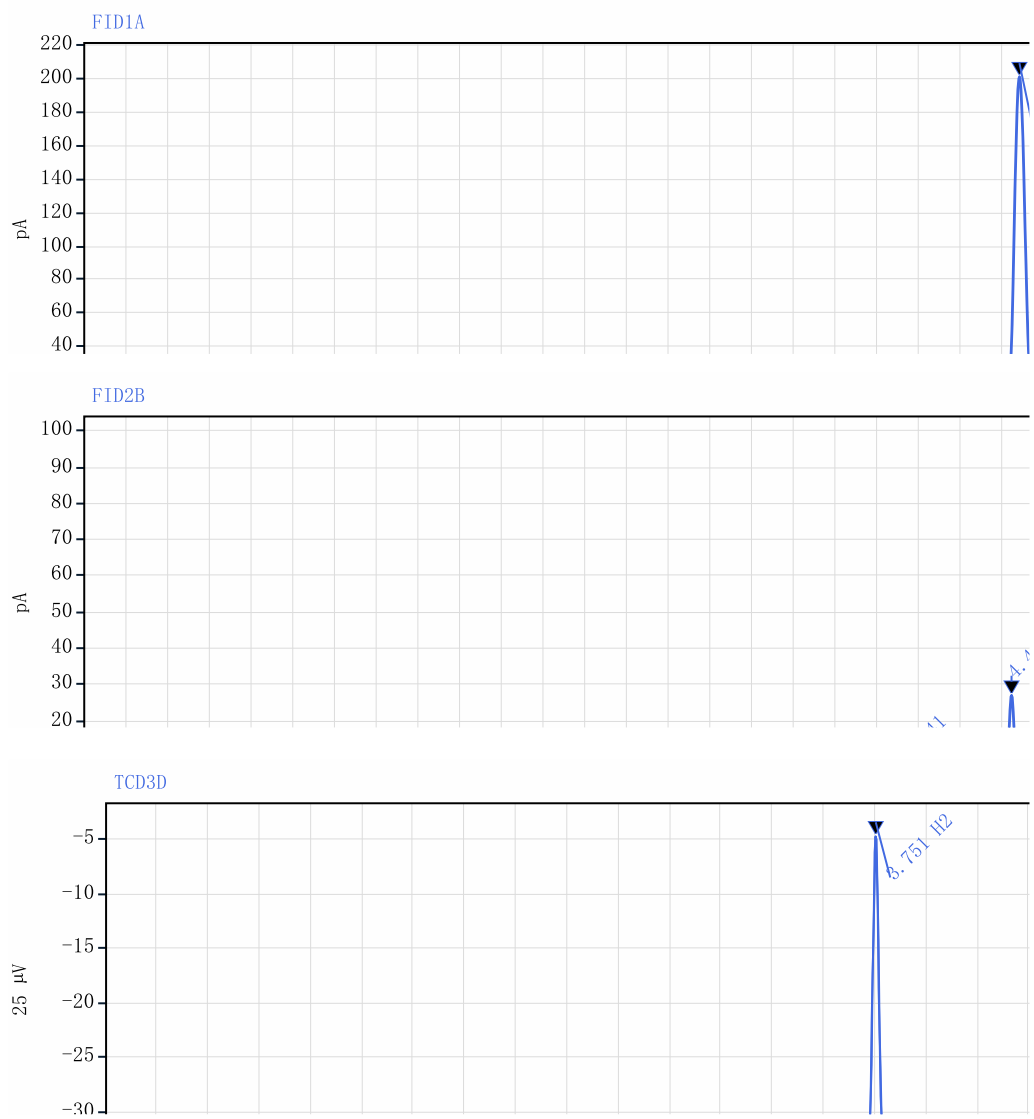

Figure S7. Representative GC-FID and GC-TCD chromatograms of CuO NSs.

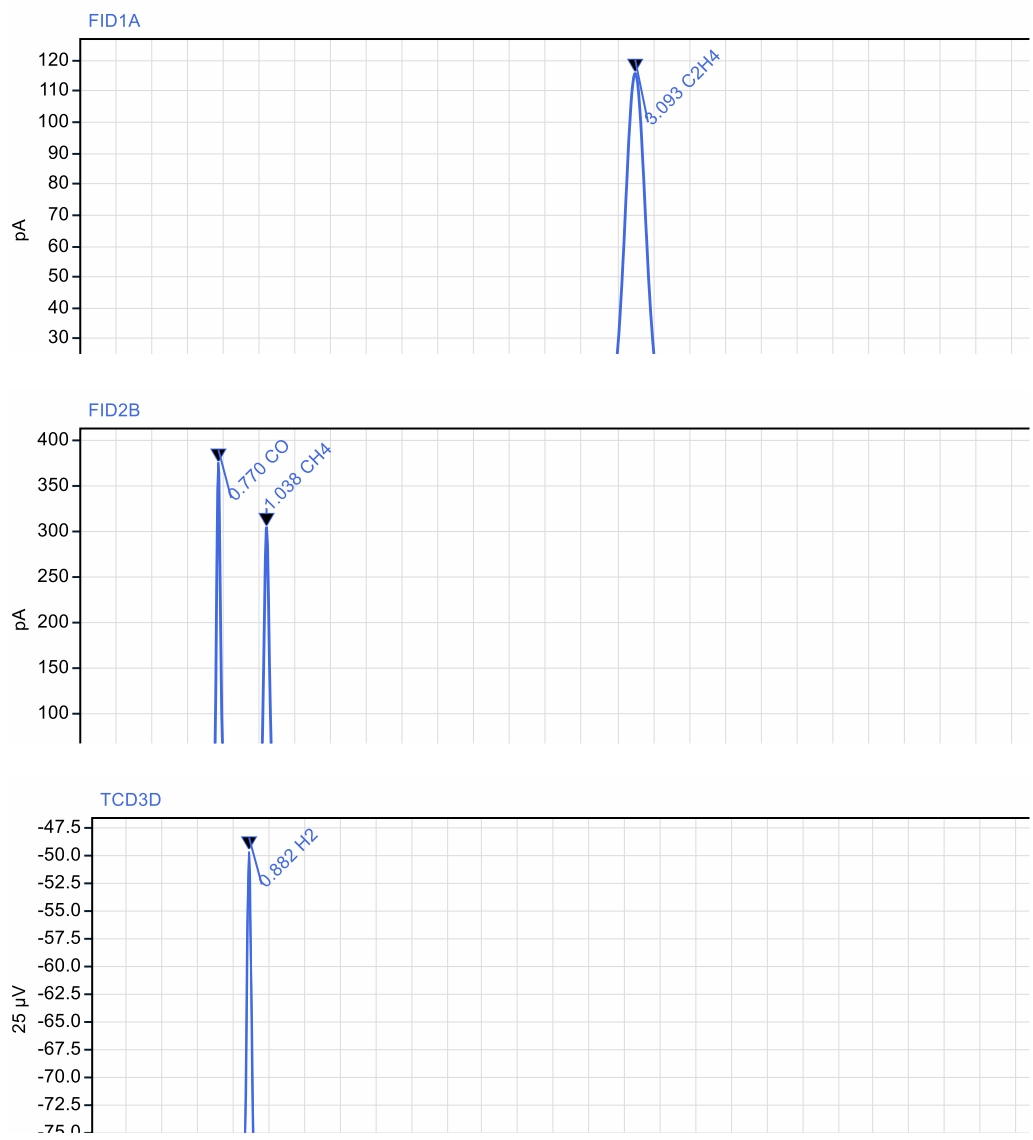

Figure S8. Representative GC-FID and GC-TCD chromatograms of CuO SPs.

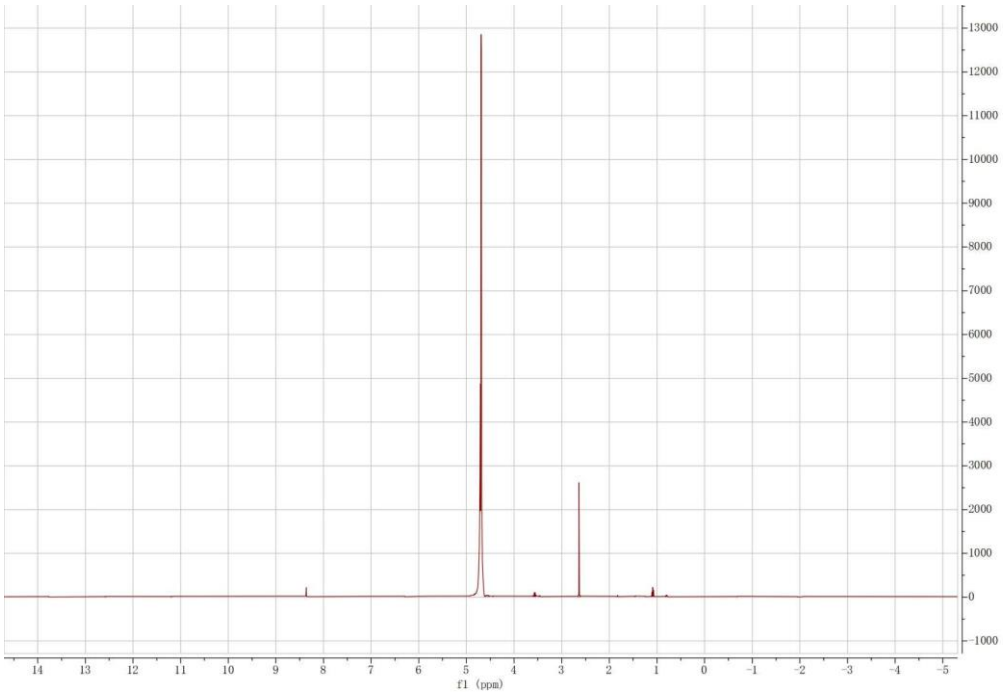

Figure S9. Representative ^{1}H NMR spectrum for the liquid solution of CuO/g-C_3N_4 that collected after 2 h CO_2RR.

Table S1. Fitting results of Tafel slope curves of CuO SPs, CuO NSs and CuO/g-C_3N_4 in CO_2-saturated $KHCO_3$ solution.

Electrode	Slope value	Standard error of slope	Intercept value	Standard error of intercept	R^2
CuO/g-C_3N_4	0.01719	0.00265	0.35492	0.00405	0.91350
CuO NSs	0.02781	0.00301	0.32184	0.00301	0.93425
CuO SPs	0.03361	0.00389	0.27414	0.00583	0.92555

Table S2. Parameters of EIS equivalent circuit of CuO SPs, CuO NSs and CuO/g-C_3N_4 in CO_2-saturated $KHCO_3$ solution.

Electrode	R_s (ohm)	R_{et} (ohm)	W ($S*s^{0.5}$)	CPE ($S*s^a$)	a
CuO/g-C_3N_4	40.65	361.8	$6.539*10^{-3}$	$101.0*10^{-6}$	0.8251
CuO NSs	45.89	702.5	$1.169*10^{-3}$	$70.96*10^{-6}$	0.8445
CuO SPs	43.45	1722	$0.296*10^{-3}$	$8.731*10^{-6}$	0.8547

Table S3. Fitting results of capacitive current of CuO SPs, CuO NSs and CuO/g-C_3N_4 at OCP.

Electrode	Slope value	Standard error of slope	Intercept value	Standard error of intercept	R^2
CuO/g-C_3N_4	0.05572	0.00319	1.96813	0.24813	0.98709
CuO NSs	0.03931	0.00124	0.74973	0.09668	0.99603
CuO SPs	0.02306	0.00101	1.1912	0.07902	0.99231